A UNIQUE EXPERIMENTAL TOOL FOR THE EVALUATION OF GAS TRANSPORT AND INTERNAL-REFORMING CHEMISTRY WITHIN SOLID OXIDE FUEL CELL ANODES

by

Amy E. Richards

A thesis submitted to the Faculty and the Board of Trustees of the Colorado School of Mines in partial fulfillment of the requirements for the degree of Master of Science (Engineering).

Golden, Colorado
Date 4/13/10

Signed: ______________________
Amy E. Richards

Signed: ______________________
Dr. Neal P. Sullivan
Thesis Advisor

Golden, Colorado
Date 4/14/2010

Signed: ______________________
Dr. Terrence E. Parker
Professor and Head
Department of Engineering

ABSTRACT

Solid-oxide fuel cells (SOFC) have generated interest due to their ability to efficiently convert the chemical energy within hydrocarbon and biomass fuels into electricity. However, the propensity for carbon-deposit formation and subsequent catalyst deactivation limits the range of SOFC operating windows. Developers are taking many different approaches to solving these problems. Numerous anode materials and architectures are being developed and tested. It is difficult to discern specific information about anode gas transport and internal-reforming chemistry using traditional electrochemical-performance tests, as these are conducted on full cells. During testing, anode processes are masked by SOFC electrochemical processes such as charge transport and charge-transfer chemistry.

Gas transport and internal-reforming properties are central to an anode's ability to operate successfully on hydrocarbon or biomass fuels. This study decouples anode chemistry processes from the electrochemistry processes present in the operation of an SOFC through the use of a unique experiment. In the Separated Anode Experiment (SAE), a single SOFC anode channel is simulated by sealing an anode between two ceramic manifolds into which flow channels have been machined. Gases representative of SOFC fuel streams are fed into the "fuel channel", while gas mixtures representative of the products of electrochemistry (H_2O and CO_2) are fed into the "electrolyte channel". Gases from these two channels are then free to cross-diffuse through the porous anode and participate in internal-reforming reactions. Exhaust-gas compositions are measured with a mass spectrometer and are used to infer details regarding the anode's gas transport and internal-reforming activity.

Five different materials and structures are compared in this study on the basis of their gas-transport and internal-reforming behavior. These materials are a CoorsTek, Inc. reaction-sintered Ni-YSZ ("RS-Type"), a traditional Ni-YSZ with anode func-

tional layer ("C-Type"), an inert YSZ barrier layer, a CoorsTek Ni-YSZ and barrier bi-layer anode, and a next-generation perovskite anode.

The Separated-Anode Experiment has been used to compare the performance of the five different anode structures described above. Through use of the Separated Anode Experiment, the RS-Type anode was found to have the highest gas transport and internal-reforming capabilities. The C-Type anode had low gas transport and internal reforming. The bi-layer anode had decreased transport when compared to the RS-Type anode due to the tighter pore structure of the barrier layer. While the perovskite anode had the second-highest gas transport capabilities, very little reforming activity was found. These results can be used to provide insight into the design of improved anodes and architectures.

TABLE OF CONTENTS

LIST OF FIGURES

LIST OF TABLES

LIST OF SYMBOLS

Pore radius	r_p
Particle diameter	d_p
Porosity	ϕ
Tortuosity	τ_g
Density	ρ
Mean Flow Velocity	u
Species Molecular Flux	J_k
Species Molecular Weight	W_k
Specific Area of Catalyst	A_s
Permeability	B_g
Viscosity	μ
Molar Production Rate	$\dot{s}_k$
Molar Concentration	X_k
Multicomponent Diffusion Coefficient	$D_{k\ell}^{\mathrm{e}}$
Knudsen Diffusion Coefficient	$D_{k,\mathrm{Kn}}^{\mathrm{e}}$

LIST OF ABBREVIATIONS

Solid Oxide Fuel Cell	SOFC
Triple-Phase Boundary	TPB
Ceramic-metallic	Cermet
Yttria-Stabilized Zirconia	YSZ
$La_{0.75}Sr_{0.25}Cr_{0.5}Mn_{0.5}O_{3-\delta}$	LSCM
$La_{0.75}Sr_{0.25}Cr_{0.5}Fe_{0.5}O_{3-\delta}$	LSCF
Electrochemical Impedance Spectroscopy	EIS
Colorado Fuel Cell Center	CFCC
Dusty Gas Model	DGM
Catalytic partial oxidation	CPOX
$Sr_{0.8}La_{0.2}TiO_3$	SLT

ACKNOWLEDGEMENTS

This work has been funded by the U.S. Department of Energy, Office of Energy Efficiency and Renewable Energy, DOE Contract DE-FG36-08GO88100. I would like to thank the Department of Energy for allowing me this opportunity. I also gratefully acknowledge Professor Neal Sullivan for his help, guidance, and friendship. I thank Professor Robert Kee and Professor Anthony Dean, both for their guidance and for serving on my thesis committee. This thesis could not have been completed without the aid of Dr. Huayang Zhu, who provided modeling support, and Dr. John Chandler, who provided assistance in the EM Lab. I would like to give a special acknowledgement to my parents, Liz and Bill Gray, for all of the opportunities and encouragement they have provided me with through the years. Last, but certainly not least, I want to thank my husband, Travis, for his constant, selfless, support and encouragement.

CHAPTER 1

INTRODUCTION

1.1 Background

Solid oxide fuel cells (SOFCs) are devices which efficiently convert fuel sources to electricity via electrochemical reactions. Due to high operating temperatures, SOFCs are able to operate on a wide variety of fuel sources, including hydrocarbon and biomass, through internal reforming. Figure 1.1 illustrates the processes underway within an SOFC.

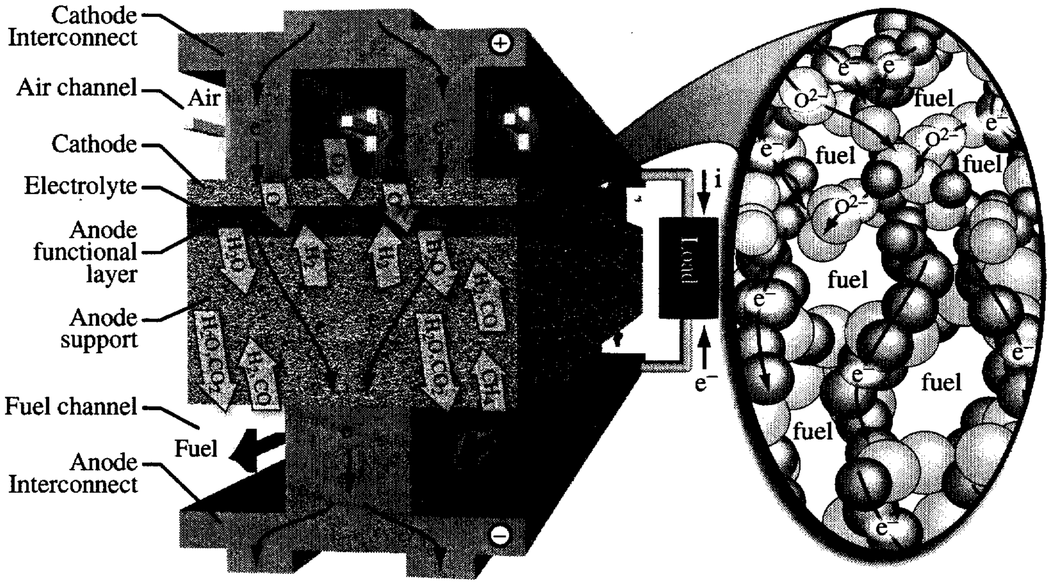

Figure 1.1: SOFC diagram and processes.

First, oxygen diffuses from the air channel through the cathode where it is reduced electrochemically to oxygen ions:

$$1/2O_2 + 2e^- \rightarrow O^{2-}.$$

The oxygen ions then diffuse through the electrolyte to the Triple-Phase Boundary (TPB) where they participate in electrochemical reactions with H_2 to produce steam and electrons,

$$2O^{2-} + H_2 \rightarrow H_2O + 2e^-.$$

The electrons are harvested to provide electricity. The steam diffuses back through the anode to participate in internal reforming reactions with hydrocarbon fuels, shown in Figure 1.1 as CH_4. The steam reforming reaction for CH_4 is

$$CH_4 + H_2O \rightarrow 3H_2 + CO.$$

Dry reforming, which utilizes CO_2, also occurs within the anode of an SOFC,

$$CH_4 + CO_2 \rightarrow 2H_2 + 2CO.$$

These reforming reactions produce syngas (H_2 and CO) to be utilized in electrochemical reactions within the TPBs.

The traditional SOFC anode material consists of a ceramic-metallic (cermet) composed of nickel and yttria-stabilized zirconia (YSZ) [1]. Ni-YSZ anodes are suitable for fuel cells because they are excellent electronic conductors and catalysts for hydrocarbon reforming. However, nickel is also a catalyst with a high propensity for carbon deposition, or coking. When coking occurs on the surface of the anode, it leads to performance degradation and eventual catalyst deactivation or cell destruction.

Many factors play a role in carbon formation within SOFCs, including but not limited to operating temperature, current density, anode material composition and morphology, parent fuel composition, and SOFC current density. Higher hydrocarbon fuels as well as liquid fuels have higher propensities for carbon formation. To counter this problem, reforming agents such as steam, air, or CO_2 may be added to the fuel stream, but decrease the overall efficiency of a system. Since higher current densities result in higher rates of steam and CO_2 generation, the current density at which a cell is operating affects carbon deposition. Higher current densities limit coking, but it is not always possible or desired to operate a system at high currents. In order to overcome these difficulties with Ni-YSZ, SOFC researchers have been working to develop new anode materials and architectures. The electrochemical performance of some of these new anodes rivals that of traditional cells, reflecting the great promise that these approaches hold. Fundamental gas-transport and internal reforming characteristics of these anodes, however, are not well understood. This lack of understanding is the primary motivation behind this study.

1.2 Objective

During SOFC operation, many coupled and competing processes occur. It is difficult to focus on gas transport and internal-reforming chemistry within an anode when so many other electrochemical processes are underway. Oxygen-reduction reactions, ionic and electronic transport, and other simultaneous processes can cloud anode-specific processes. Traditional electrochemical tests like polarization measurements or electrochemical impedance spectroscopy can provide a broad comparison of cell performance, but SOFC processes mask anode-reforming and gas-transport processes.

The objective of this work is to develop and demonstrate an experimental tool that may be used to compare new anodes based solely on processes occuring within the anode by decoupling these processes from electrochemical processes. Understanding gas-transport and internal reforming in these anodes is an important step in comparing their potential for replacing the traditional anode. Furthermore, this knowledge can be used to optimize design of advanced materials and structures.

1.3 Approach

The Separated Anode Experiment (SAE) has been previously developed to decouple thermochemical processes from SOFC electrochemical processes [2, 3]. It has been further improved upon and validated in this work. Together with morphological characterization, it is used to compare and understand five different anode materials and architectures. These anodes include a CoorsTek reaction-sintered Ni-YSZ anode "RS-Type"), a traditional Ni-YSZ anode with an anode functional layer (AFL) ("C-Type"), an RS-Type anode combined with an inert YSZ barrier layer, and a nickel-free perovskite anode. To separate chemistry and gas transport in the barrier layer from those processes in the RS-Type anode, a barrier layer is also analyzed separately.

CHAPTER 2

BACKGROUND

Previous studies have taken many different approaches to overcoming the obstacles preventing a broader application of SOFCs. Much has been done in the area of materials development to produce an anode with the ability to operate well on hydrocarbon fuels without the problem of carbon deposition. Additionally, many types of tests have been applied to broaden the robustness and general understanding of SOFC anodes. These approaches are briefly reviewed below.

2.1 Materials Development

In efforts to overcome the problems of carbon-deposition and subsequent catalyst deactivation, SOFC developers have taken numerous approaches. These include variations on the architectures of traditional Ni-YSZ cermets and attempts to use completely nickel-free perovskite or metallic anodes.

2.1.1 Inert-Barrier and Active-Catalyst Layers

Many of the variations being made on the traditional Ni-YSZ cell include changes to the cell's architecture. A chemically-inert, porous barrier layer (YSZ) positioned between the fuel stream and a traditional Ni-YSZ anode (see Figure 2.1) impedes the flux of fuel onto the anode surface while slowing down the flux of CO_2 and H_2O into the fuel compartment. It thus traps the electrochemistry products increasing H_2O and CO_2 concentrations within the anode structure, promoting deposit-free internal reforming.

Lin et al. found that the utilization of a barrier layer decreased the current density at which a cell could be operated without coking [4]. The fuel used was CH_4 and polarization measurements were performed on cells with and without added barrier layers. The critical current density was 1.8 A/cm^2 for the cell operated without a barrier layer and was 0.6 A/cm^2 for the cell with a barrier layer. Thus, wider operation windows exist for cells combined with inert barrier layers.

Barrier layers have shown promise in fuel cell testing where CH_4 - CO_2 and CH_4 - air mixtures were used as the fuel supply [5]. They were found to increase the stability of the cells via mitigation of carbon deposition and by slowing endothermic reactions which would normally lead to cell cracking. The addition of CO_2 and air to the CH_4 fuel streams allowed for wider operating windows.

A computational study performed by Zhu et al. further shows that barrier layers assist in increasing the stability of Ni-YSZ cells [6]. The computational model includes heterogeneous reaction chemistry and porous-media transport. The work also shows that a barrier layer can lead to coke-free operation for a longer tubular SOFC.

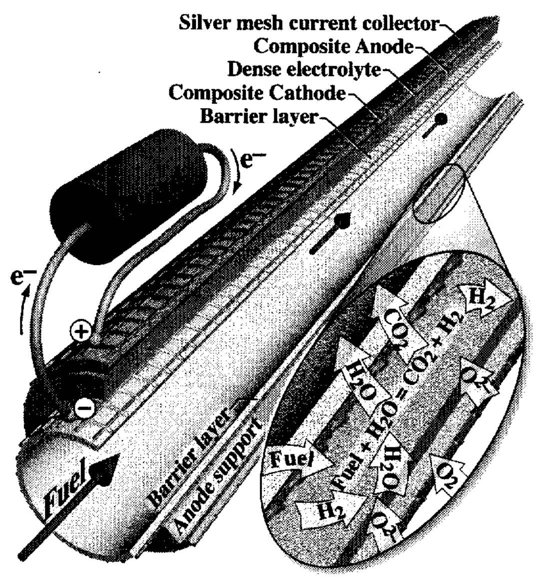

Figure 2.1: Illustration of barrier layer placement and function.

Building upon the use of barrier-layer architectures, developers have added active metal catalysts to the porous barrier layer, making it catalytically active. Zhan and Barnett applied a thin layer of Ru-CeO_2 to a porous YSZ disk which was placed between the anode and fuel stream [7]. Stable results were acheived for the fuel cell operating on *iso*-octane. Some coking was observed, but results were promising.

Cheekatamarla et al., of NanoDynamics Energy, Inc., had success with a catalyst layer on top of a Ni-YSZ anode [8]. The composition of the catalyst was undisclosed for proprietary reasons. Natural gas, biogas, and propane were reformed via catalytic partial oxidation (CPOX) over the anode without coke formation.

2.1.2 Perovskite Anodes

Perovskite anodes are being explored as an alternative to Ni-YSZ anodes. Perovskites are an electronically conductive ceramic with the generic structure ABO_3, where A and B are cations (see Figure 2.2). Many different combinations of A- and B-site dopants exist and are chosen to meet specific application requirements. For fuel cells operating on hydrocarbon fuels, a large focus has been placed on materials of the form $LaCrO_3$ due to their stability at high temperatures and in the presence of low oxygen partial pressures [9]. $LaCrO_3$ is doped on both the A and B sites to increase catalytic activity for hydrocarbon reforming.

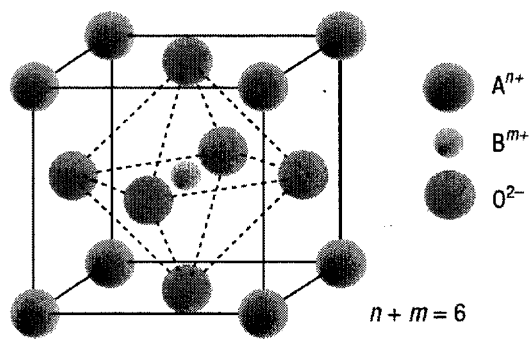

Figure 2.2: Unit cell of the ABO_3 perovskite structure [10].

Tao and Irvine performed testing in hydrogen and methane with an $La_{0.75}Sr_{0.25}Cr_{0.5}Ma_{0.5}O_3$ (LSCM) anode on an electrolyte-supported cell [11]. When tested in hydrogen, performance was comparable to that of a cell with a Ni-YSZ anode. Open circuit voltage and maximum power density were, as expected, lower when the cell was operated on methane. After seven hours of testing in CH_4, only trace amounts of carbon were found to be deposited on the anode by thermal-gravimetric analysis (TGA). The relative contributions of direct oxidation and internal reforming responsible for utilization of the methane fuel are unclear.

Bastidas et al. have shown LSCM to be stable when used as both the anode and cathode of a cell [12]. Maximum power densities for operation in hydrogen and methane were lower than those achieved by the cells tested by Tao and Irvine, but many variables could have contributed to this fact. Reduction/oxidation (redox) stability was investigated by cycling in reducing and oxidizing environments five times and testing polarization resistance after each cycle. Only small changes were observed in the polarization impedance plots, thus demonstrating the redox stability of this material.

Porous YSZ anodes were impregnated with LSCM by Corre et al. [13]. When exposed to fuel, the microstructure reveals a nanoparticle network resulting in a long triple-phase boundary (TPB). This idea is attractive because all electrochemical reactions occur at within the TPB. However, interactions between the LSCM and YSZ scaffold cause a reduction in conductivity as the microstructure evolves over time.

In an attempt to understand the catalytic mechanism occuring during utilization of LSCM-based anodes under methane fuel, Bruce et al. [14] performed testing on LSCM- and Cu-impregnated YSZ anodes. Copper was added for increased electronic conductivity. Current-voltage and impedance curves were obtained for operation gases of H_2, CH_4, and C_4H_{10}. The amounts of CO, CO_2, and H_2 in the fuel cell effluent gas were measured with a gas chromatograph (GC) and impedance spectra were obtained for current densities varying from 0 to 200 mA/cm^2. It was concluded that at open-circuit conditions, the reaction mechanism for hydrocarbon fuels is dominated by cracking reactions. At higher current densities, LSCM becomes active for total hydrocarbon oxidation. The processes in an LSCM anode are highly dependent on the oxygen ion flux through the electrolyte.

The abilities of $La_{0.75}Sr_{0.25}Cr_{0.5}Fe_{0.5}O_{3-\delta}$ (LSCF) to catalyze methane reforming and perform electrochemically were analyzed by Tao and Irvine [15]. Catalytic activity was evaluated using LSCF powder in a fixed-bed reactor. Impedance spectroscopy was used to evaluate electrochemical performance. Although catalytic activity was decent at temperatures higher than 900°C, electrochemical performance was lower than that of LSCM.

Fu et al. [16] and Ovalle et al. [17] have investigated a family of perovskite titanates ($La_4Sr_8Ti_{12-x}Mn_xO_{38-\delta}$) for use as fuel cell anodes. The first group found poor performance at a temperature of 856°C, but the latter group found good performance at 950°C. It is possible that these anodes may require a higher temperature of operation than the standard Ni-YSZ anode which operates at 800°C. These results were based on polarization resistance data.

Pillai et al. have developed anodes consisting of a conducting support of $Sr_{0.8}La_{0.2}TiO_3$ (SLT) with a Ni-YSZ electrochemically active layer [18]. During long-term testing, SOFCs with this anode were stable for eighty hours while operating on natural gas.

Other perovskite anodes being developed and explored are $La_{0.8}Sr_{0.2}Sc_{0.2}Mn_{0.8}O_3$ (LSSM) [19], Nb-doped $SrTiO_3$ [20], La-substituted $SrTiO_3$ [21], and $Sr_2MgMoO_{6-\delta}$ [22]. In addition to the materials listed above, many other perovskite-based anodes are being developed and tested in similar methods.

2.1.3 Metallic Anodes

Another nickel-free type of anode being developed is the metallic anode. Copper has been the main focus of these efforts.

Anodes composed of 40wt% Cu and 20wt% CeO_2, held in place by a YSZ matrix, were tested on hydrogen and *n*-butane by Park et al. [23]. While Cu is an excellent electronic conductor, it is a poor catalyst for C-H bond activation. Carbon formation is thus avoided with Cu anodes, but additional catalytic activity for hydrocarbon reforming is needed. Ceria is used here to increase this catalytic activity. Maximum power densities were 0.31 W cm^{-2} and 0.18 W cm^{-2} for hydrogen and n-butane, respectively. No change in performance was observed during a testing period of 48 hours in dry butane. In a study by the same group, multiple formulations of a Cu-Ceria-YSZ anode were tested and it was determined that the method of fabrication has a large effect on cell performance [24].

Kim et al. performed a study aimed at understanding the mechanism of carbon deposition on Cu-Ceria-YSZ anodes and methods for avoiding it [25]. While carbon does form on Cu when using n-decane, toluene, or naptha, it only deactivates the reaction by filling in the pores. The copper surface does not participate in the carbon-forming reaction. It is thus easier to remove and the surface may be regenerated, unlike carbon deposition on Ni which causes the electrode to fracture. It was also determined that a layer of ceria on top of the Cu surface allows carbon to be removed by reaction with steam as quickly as the carbon forms.

By means of a density functional theory study, Galea et al. found that, when compared to Cu anodes, Cu-Ni and Cu-Co alloys have increased activity [26]. The reason for increased activity is exposure of the Ni or Co surfaces. Decreased carbon formation is also observed due to blocking of specific Ni sites.

The catalytic properties of Cu and Cu-Ni anodes combine with Ce, Ce-Tb, and Ce-Gd have been studied by Hórnes et al. [27]. With respect to oxidation of methane, higher catalytic activity was observed in the presence of Tb or Gd dopants in ceria, even when no Ni was present.

Lee et al. tested Cu-Ni and Cu-Co systems under H_2 and n-butane at 973 K and 1073 K [28]. At 973 K, the addition of Ni or Co to Cu anodes increased performance in H_2 but had no effect on testing in butane. At 1073 K, however, which is the standard SOFC operating temperature, increases in performance were observed for both fuels. The authors concluded that bimetallic anodes are worth considering for use in SOFCs. Similarly, the same group thoroughly investigated Cu-Co anodes for use with CH_4 [29]. Only small amounts of carbon were found following exposure to CH_4 at 1073 K for 2 h, even in anodes with 90 wt% Co. A cell with a 50:50 ratio of Cu and Co was found to be stable in humidified CH_4 at 1073 K for 500 h.

Symmetrical cells composed of (Ni,M)/YSZ cermets on either side of a YSZ electrolyte were fabricated and tested by Ringuedé et al. [30]. Co, Cu, and Fe were used as the metal dopants. On the basis of impedance spectroscopy measurements, the best performance was obtained for the $Ni_{1-x}Co_x$/YSZ cermet.

Grgicak et al. have taken a closer look at different combinations of $Ni_{1-x}Co_x$/YSZ and $Ni_{1-x}Cu_x$/YSZ anodes [31]. Of the anodes tested, $Ni_{0.92}CO_{0.08}$ had the highest performance. The high performance was attributed to a lengthening of the TPB. Impedance measurements and exchange current measurements in H_2, CH_4, and H_2S/CH_4 were used as a basis for comparison.

2.2 Experimental Methods

As evidenced in the previous section, many different anode materials are currently being developed and evaluated for use in SOFCs. Unfortunately, no standardized method for testing the ability of a material to operate with hydrocarbon fuels is used in the literature. Electrochemical-performance tests are used in the majority of studies. These include polarization measurements (current-voltage curves) and electrochemical impedance spectroscopy (EIS) [1,32]. While useful, these tests do not enable focus on the gas-transport and thermal-chemistry processes that are critical in understanding internal-reforming behavior. These tests provide information on the entire cell performance and, in addition to being dependent on the new anode material, are also dependent on the other components of the cell. Interfaces between the anode and electrolyte and the electrolyte and cathode play a large role, as does the quality of the electrolyte and cathode. While EIS aids in isolating the performance of different cell components, it does not provide information regarding the material and catalytic properties of an anode.

Optical *in-situ* techniques have been used to characterize anode processes. Sukeshini et al. focused on electrochemical oxidation in patterned Ni anodes [33]. Anode chemistry [34,35] and carbon-deposit formation [36] have also been analyzed using optical techniques . These tests, however, are limited to observation of the anode surface and do not address the tightly-coupled relationship between gas transport and reforming chemistry within the anode.

The lack of focus placed on thermochemistry within anode structures provides the primary motivation for this work. While extensive research has been conducted to improve the performance of SOFC anodes on hydrocarbon fuels, the previous work of Hecht et al. [2] is the only one to isolate thermochemistry from electrochemistry within the structure of an SOFC anode. The research described in this thesis builds on and extends this previous effort.

CHAPTER 3

EXPERIMENTAL METHOD

Five different anodes and architectures are fabricated, analyzed, and compared in this study using a number of techniques. They are a CoorsTek reaction-sintered Ni-YSZ anode (RS-Type), a more-conventional Ni-YSZ anode fabricated using commercially-available ceramic powders (C-Type), a YSZ barrier-layer, a combination of the RS-Type anode and the barrier layer (bi-layer), and a nickel-free next-generation perovskite anode (LSCM). Analysis techniques include liquid picnometry (Archimedes' Method) for determination of porosity, mercury porosimetry, and SEM image analysis. Finally, the Separated Anode Experiment (SAE) is used to compare gas transport and internal-reforming chemistry performace.

3.1 Anode Fabrication

The five different anodes tested in this work are fabricated using the methods described below. All anodes are processed via powder processing techniques or cast using a slurry. They are then sintered at the temperatures indicated prior to experimental testing.

3.1.1 CoorsTek Reaction-Sintered Ni-YSZ Anode

The benchmark anode for this study is the Ni-YRSZ anode developed by CoorsTek, Inc [37]. Powder preparation begins by combining and ball-milling 92 mol% monoclinic zirconia powder with 8 mol% yttria powder (Advanced Material Resources, Toronto, Ontario). The yttria-zirconia powder is dried and screened, then blended with 65 wt% nickel oxide (OMG, Westlake, OH). The anode powder is then mixed with a binder specific to the desired anode-forming process, which in this case is dry-pressing. No pore former is added. The slurry is spray-dried into a rotary atomizer.

The RS-based NiO powders have a particle size of 10 μm. Powders are prepared at CoorsTek, Inc. and are provided to the Colorado Fuel Cell Center (CFCC).

At the CFCC, the powder is weighed into 10-g portions and pressed into disc-shaped compacts using a uni-axial press (Carver AutoFour30) loaded to 53.4 kN (12000 lb) with a 10-s hold time. The compacts are placed onto YSZ-Al_2O_3 porous setter plates (Selee Ceramics) and sintered in air at a temperature of 1400°C for four hours [38]. After sintering, the anode measures 4.43 cm (1.74 in.) in diameter and is 1.45 mm (0.057 in.) thick. This anode is designated as "RS-Type" throughout the remainder of this thesis.

3.1.2 Conventional Anode

The conventional anode contains an additional anode functional layer (AFL). An AFL is a thin layer on top of the anode that is less porous than the bulk material. Fabrication begins by combining 50 wt% NiO and 50 wt% Tosoh YSZ powders together with a solvent. The solution is ball milled for 24 hours with 10% starch pore former and 1% PVB binder. After milling, it is dried and dry sieved to -325 mesh. The powder is then pressed and bisque fired to 1000°C. The AFL consists of the same powder without pore former and is applied via screen printing to the bisque-fired anode. The assembly is sintered at 1400°C for four hours and results in a 20-μm-thick AFL on top of the 866.4-μm-thick (0.034 in.) support. Final anode dimensions are a 4.81 cm (1.89 in.) diameter with a thickness of 0.886 mm (0.035 in). This anode is designated as "C-Type" throughout the remainder of this thesis.

3.1.3 YSZ Barrier Layer

The YSZ barrier layer is fabricated by combining 95.2 wt% YSZ (Unitec, UK) with 4.76 wt% pore former along with DI water and dispersant (Darvan 821A, Norwalk, CT). The mixture is ball-milled for 24 hours. Binder (Mohr Mate) is added and the solution is ball-milled for a second time for up to four hours. The slurry is cast into a 6.35-cm (2.5 in.) PVC mold sprayed with mold release and allowed to dry. The resulting disc is sintered at 1450°C for one hour. The final diameter of the barrier layer disc is 5.92 cm (1.74 in.) and the thickness is 0.95 mm (0.037 in.).

3.1.4 RS-Type/Barrier Bi-Layer

To test the combination of the YSZ barrier layer with the Ni-YRSZ anode (bi-layer), the barrier layer disc is simply placed on top of the Ni-YRSZ anode.

3.1.5 LSCM Anode

To obtain a powder suitable for dry pressing, 100 parts LSCM powder (Fuel Cell Materials, Lewis Center, OH) is formed into a slurry by adding 1.5 parts dispersant (Darvan C) and 45 parts DI water. A binder is added and the resulting slip is pan-dried. The dried powder is crushed with a mortar and pestle and screened to -60 mesh. The powder is pressed by weighing out 10 grams of material and pressing into a disc-shaped compact with a uni-axial press, the same process as used for fabricated Ni-YRSZ discs. The LSCM discs are sintered at 1300°C for 10 hours. After sintering, the LSCM discs measure approximately 4.5 cm (1.77 in.) in diameter and 1.11 mm (0.044 in.) in thickness.

3.2 Separated Anode Experiment

The Separated Anode Experiment (SAE) was designed and fabricated to provide a means for decoupling anode-reforming processes from electrochemical processes. The experiment was previously fabricated and used by several members of our group as outlined in Hecht et al. [2, 39], Daggett [3], and Gupta [40]. A second SAE was built for this study. Major modifications to the previous designs include: 1) the utilization of chemically inert ceramic manifolds and tubing inside the hot zone, 2) alternate sealing method, 3) revised startup procedures, and 4) revised procedures for measuring gas composition.

3.2.1 Design

An illustration of the SAE is shown in Figure 3.1. The anode is placed between two alumina manifolds into which flow channels have been machined. Mica sheets with flow-channel cutouts are placed between the anode and manifolds. The anode is sealed into the manifold using alumina paste (Cotronics 989FS) applied around the edges. The entire assembly is placed into a furnace and compressed to achieve further sealing. Within the furnace, the anode is heated to SOFC operating temperatures (800°C). While a range of temperatures can be used in testing, only one temperature set-point is used in this study. An inlet tube on the fuel-side (top) is fed with gases representative of SOFC fuel mixtures. The electrolyte-side (bottom) inlet tube is fed with gases present at the SOFC triple-phase boundaries. Mass flow controllers (Alicat Scientific) are used to feed gases to the manifold assembly. Thermocouples are placed at the surface of the anode to monitor temperature.

As fuel-stream and electrolyte-stream gases cross-diffuse through the anode material in opposing directions, they are free to heterogeneously react with each other in catalytic reforming reactions to produce hydrogen, carbon monoxide, and other species. These species then diffuse back to the flow channels on either the fuel- or electrolyte-side, are carried into the outlet tubes. Exhaust gas compositions are measured using a mass spectrometer (Stanford Research Systems RGA 200). Prior to reaching the mass spectrometer, steam is condensed out of the exhaust streams using a counterflow dryer with an internal Nafion membrane (Perma Pure MD Series). In this dryer, the exhaust sample stream flows through the tube in one direction while dry air at slightly lower pressure flows counter to the sample stream. The steam contained in the sample stream is transported across the Nafion membrane to the dry-air stream, so that a water-free gas sample is provided to the mass spectrometer (MS) for analysis.

As no electrolyte or cathode is present in this apparatus, the design decouples anode gas-transport and reforming processes from electrochemical processes. The design of the SAE enables focus to be placed on an anode's ability to promote internal reforming reactions.

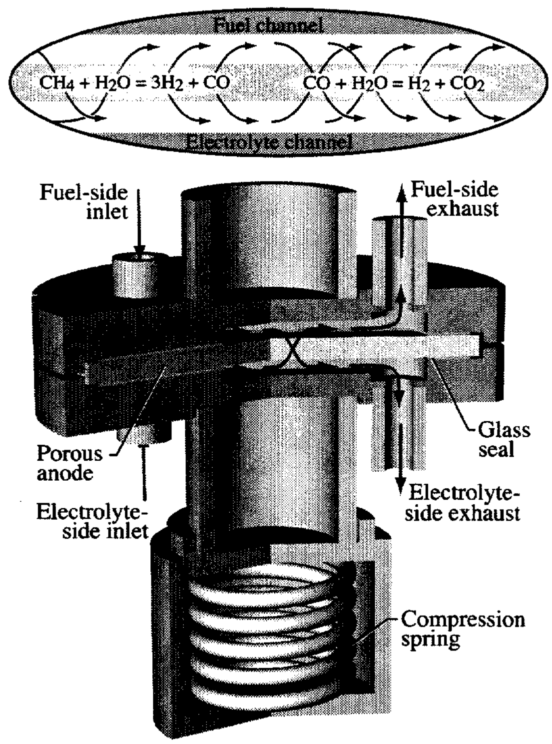

Figure 3.1: Cutaway illustration of the SAE anode assembly.

3.2.2 Ceramic Manifolds

A major improvement to the design of the SAE is the employment of alumina manifolds and tubing in place of the Inconel and stainless steel assembly used in prior studies. The purpose of this alteration is to eliminate catalytic reactions of the gases with the tubing and manifold. Since the tubing and manifold are present in the hot zone of the furnace along with the anode material, temperatures are sufficiently high to activate chemical reactions in the presence of a catalytic surface. Alumina is a more inert material than steel, and thus does not promote catalytic reactions. Any reactions that occur result from contact with the anode itself or are due to gas-phase chemistry. The manifolds each contain a 0.635 cm (0.25 in.) wide and 2.9 cm (1.14 in.) long flow channel and were manufactured by O'Keefe Ceramics in Woodland Park, Colorado. A technical drawing of the manifold is included in Appendix A. The 0.635 cm (0.25 in.) tubes (CoorsTek, Inc.) are sealed to the manifold with alumina paste (Cotronics 989FS) after careful machining of the manifolds to match ceramic-tube diameters.

3.2.3 Measurement Methods

Measurements of the exhaust-gas compositions are taken with a Stanford Research Systems RGA 200 quadrapole mass spectrometer. Daily calibrations are performed on the instrument prior to testing to increase the accuracy in quantifying mole fractions of argon, hydrogen, methane, carbon dioxide, and carbon monoxide. These are performed by sending several known gas mixtures to the mass spectrometer and plotting the resulting readings. A curve is fit to the data and the resulting slope and y-intercepts are then used to quantify mole fractions in experimental exhaust streams. Daily calibrations were determined to be necessary after long-term studies of the drift in the mass spectrometer. A single mass-to-charge ratio (m/e) is chosen from each species' cracking pattern to represent the amount of that species present in the fuel stream. Cracking patterns are obtained from the NIST Standard Database Number 69 [41]. Nominal m/e peaks used are H_2: 2; CH_4: 16; CO: 28; Ar: 40; and CO_2: 44.

An overlap exists between the CO and N_2 peaks, both of which are located at an m/e value of 28. While no nitrogen is deliberately added in these experiments, undesirable air leaks can exist. Of course, it would be desirable to eliminate all leaks, but it is not possible with the current setup of the experimental system. Leaks within the furnace have been eliminated as much as possible via sealing methods to ensure that no extra oxygen is available for combustion within the hot zone. In order to overcome the overlap of the N_2 and CO peaks, a background measurement is taken prior to testing every anode. The raw N_2 signal is normalized by the Ar signal at every flow rate and is subtracted from the subsequent experimental results. On average, the N_2 leaks are approximately 4% at 75 sccm and 1% at 200 sccm. An overlap comprised of 8.627% of the CO_2 signal is also present at an m/e of 28. It is corrected for by subtracting this percentage of the m/e value at 44 from the signal at the m/e value of 28.

Every measurement is allowed to come to steady-state over a period of 45 minutes before pressure-versus-time data are collected for five minutes. The five-minute data collection period results in 300 peaks which are averaged to obtain one peak value for each m/e value. These data are normalized by the argon signal and converted to mole fractions using calibration constants calculated from known input concentration values.

3.2.4 Start-up Procedures

To ensure complete reforming, standard operating procedure is to heat the anode under forming gas (FG), a mixture of 3.5% H_2/96.5% Ar, and then switch to a gas stream containing more hydrogen (68% H_2/32% Ar) for 48 hours. The anode is not exposed to the higher-hydrogen content gas stream during startup as this has been found to lead to cell cracking. Complete reduction is necessary for anodes containing NiO prior to performing experiments because it increases the anode porosity and exposes additional catalytic Ni surface sites for fuel-reforming processes. It was discovered through experimental studies that complete reduction of NiO to Ni takes significantly longer than originally thought.

3.3 Anode Characterization

Many materials properties strongly affect gas transport and internal reforming, including porosity, pore size, particle size, tortuosity, and catalyst surface area. To gain a complete understanding of anode structures and their ability to promote gas transport, several methods of anode characterization are utilized to complement SAE experimentation. Scanning Electron Microscopy (SEM) is used to obtain a visual understanding of the morphology of each material. Porosity (ϕ), particle diameter (d_p), and pore size (r_p) are also determined for further comprehension of gas transport performance.

3.3.1 Scanning Electron Microscopy of Anodes

Cross-sectional and surface SEM images of the anode structures are captured using a JEOL JSM-7000F Field Emission Scanning Electron Microsope. Prior to analysis by SEM, materials containing nickel oxide are exposed to a reducing environment (3.5% H_2, balance Ar) for at least 48 hours. This process converts the nickel oxide within the anode to nickel, and increases the anode porosity, more-accurately reflecting the anode microstructure during cell operation.

By utilizing SEM at a high magnification, particle size of the materials is quantitatively determined. Additionally, SEM analysis qualitatively reveals the differences between each anode material. In comparing SEM images of potential anode materials, a general understanding of how a material will perform as an anode is gained. It also serves to validate certain morphological properties and behaviors when combined with experimental results.

3.3.2 Material Properties of Anodes

In addition to mean particle size, properties necessary for representation in the model are porosity, mean pore radius, specific catalyst surface area, and overall anode

Table 3.1: Material property measurement methods.

Property	Method of Measurement
Porosity	Liquid Picnometry
Mean pore radius	Mercury Porosimetry
Mean particle size	High-magnification SEM
Thickness	Anode measurement

thickness. Porosity and mean pore radius are determined after NiO reduction using liquid picnometry (Archimedes' method) [42] and mercury porosimetry, respectively. Mercury porosimetry characterization is conducted by Micromeritics Particle Analysis (Norcross, GA). Anode thickness is determined for each anode tested by using an average of ten thickness measurements taken with calipers in random locations across the anode. Table 3.1 contains a summary of the material properties measured and the techniques used.

3.4 CO_2 Transport Experiments

To provide a relative measure of the ability of gases to diffuse through a particular anode material, gas transport experiments are performed prior to reforming experiments in the SAE.

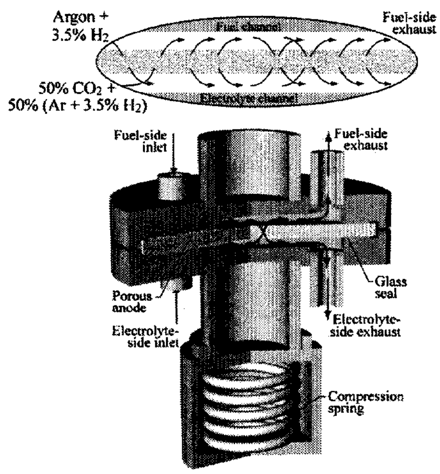

Figure 3.2: Illustration of SAE including CO_2 transport inlet gas compositions.

In these experiments, a near-inert gas stream composed of 50% CO_2 and 50% FG is fed to the electrolyte-side inlet while a stream of 100% FG is fed to the fuel-side inlet (Figure 3.2). These gas compositions are "near-inert" because CO_2 and H_2 react with each other in the gas-phase. Tests are performed at four flow rates (75, 100, 150, and 200 sccm). The amount of CO_2 transported across the anode into the fuel-side exhaust is measured with mass spectrometry. Results from these tests are used to compare gas transport across different anode structures.

3.5 Methane Dry Reforming Experiments

Fuel reforming experiments are performed utilizing a mixture of methane and carbon dioxide at a typical SOFC operating temperature (800°C). Carbon dioxide represents products of electrochemistry that would be present at the electrolyte-anode interface during typical SOFC operation. Though steam is an important product of electrochemistry, difficulties were encountered in obtaining repeatable results utilizing steam in the SAE. An evaluation of the differences between steam and dry reforming is presented in Section 5.1. As illustrated in Figure 3.3, a mixture of 20% CH_4/80% FG is supplied to the fuel-side inlet of the anode and a 50% CO_2/50% FG mixture is supplied to the electrolyte-side inlet. The gases diffuse through the porous anode and are free to participate in reforming reactions. Both the fuel-side and electrolyte-side exhaust stream compositions are measured with a mass spectrometer. As in the transport experiments, tests are performed for four different flow rates (75, 100, 150, and 200 sccm). From these results, information may be inferred about the heterogeneous chemistry processes underway within the anode with relative comparisons on the fuel-reforming properties of each type of anode material and architecture. For the selected test flow rates, a fuel utilization may be calculated and related to operation of a fuel cell. Assuming a current density of 0.45 A/cm^2, the fuel utilization based on a molar flow rate of hydrogen would be between 3.6% for the 200 sccm condition and 10% for the 75 sccm condition. These calculations assume that each mole of CH_4 fuel is converted to two moles of H_2 fuel. The actual conversion, based on reforming conditions, is much lower and translates into a higher utilization. Experimental constraints prevent the use of lower flow rates in these tests. Calculation details may be found in Appendix B.

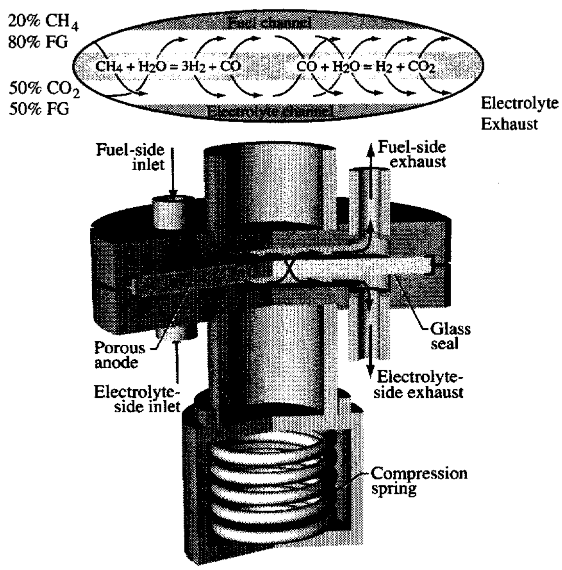

Figure 3.3: Illustration of SAE including CH_4 dry reforming inlet gas compositions.

3.6 Experimental Repeatability

Repeatability of the SAE was evaluated using a CoorsTek anode. The anode was placed into the SAE and reduced in accordance with normal startup procedures as described in Section 3.2.4. Tests were conducted over a period of three days with one full set of experiments being performed every day. The full set of experiments included mass spectrometer calibration, a CO_2 transport test, and a CH_4 dry-reforming test following the procedures described previously.

CHAPTER 4

PLUG-FLOW REACTOR MODEL DESCRIPTION

While steam is the primary product of electrochemistry during normal SOFC operation, CO_2 is substituted for H_2O in the electrolyte channel for these studies, as control of CO_2 addition is far more simple and accurate than that of H_2O addition. Clearly, this leads to changes in products formed and the extent of reforming, as steam- and dry-reforming processes differ significantly.

In order to evaluate the differences in final product composition between steam-reforming and dry-reforming, a one-dimensional model of a plug-flow catalytic reactor (Figure 4.1) is used to compare the results of each reforming approach. The model utilizes the CANTERA [43] programming package and is solved as a boundary-value problem. The gases diffuse through the catalyst material and participate in reforming reactions.

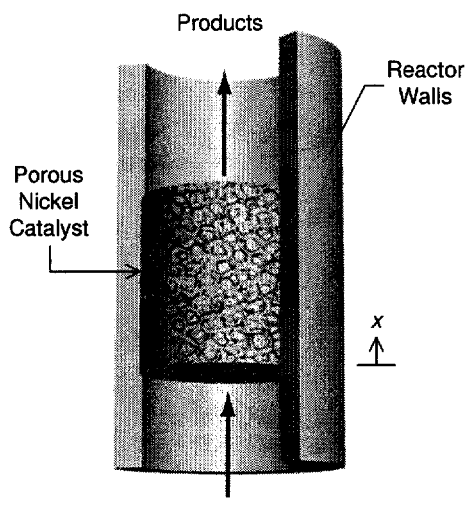

Figure 4.1: Schematic of catalytic plug-flow reactor model.

The reactor is modeled using steady-state, plug-flow assumptions. Gas-phase chemistry within the voids of the porous material is assumed to be negligible, as is gas-phase chemistry in the reactor. The one-dimensional flow within the reactor is described by the overall continuity and species equations,

$$\frac{\mathrm{d}(\rho u)}{\mathrm{d}x} = \frac{1}{D}\sum_{k=1}^{K} J_k W_k, \tag{4.1}$$

$$\frac{\mathrm{d}(\rho u Y_k)}{\mathrm{d}x} = \frac{1}{D} J_k W_k. \tag{4.2}$$

The independent variable is the length through the reactor (x) and the dependent variables are the species mass fractions (Y_k) of the K gas-phase species and mean flow velocity (u). W_k represents the species molecular weights. The diameter of the tubular reactor is D. Density (ρ) is solved for with the Ideal Gas Law. Temperatures are assumed to be uniform as set by the external furnace. The variable J_k is the normal component of the species molar fluxes across the interface of the porous catalyst material.

Exchange fluxes within the catalyst material are determined by solving a reactive porous-media problem. The catalytically reactive behavior within the material is described as

$$\nabla \cdot \mathbf{J}_k = A_\mathrm{s} \dot{s}_k, \tag{4.3}$$

where $\mathbf{J}_k$ are the species fluxes within the catalyst, A_s is the specific area (i.e., area per unit volume) of the exposed Ni catalyst, and $\dot{s}_k$ are the molar production rates of gas-phase species k by heterogeneous reforming chemistry [44].

Species fluxes within the porous catalyst are governed by the Dusty-Gas Model (DGM) [45, 46]. It is an implicit relationship between the gas-phase species molar fluxes $\mathbf{J}_k$, molar concentrations $[X_k]$, concentration gradients, and the pressure gradient p as

$$\sum_{\ell \neq k} \frac{[X_\ell]\mathbf{J}_k - [X_k]\mathbf{J}_\ell}{[X_\mathrm{T}]D^\mathrm{e}_{k\ell}} + \frac{\mathbf{J}_k}{D^\mathrm{e}_{k,\mathrm{Kn}}} = -\boldsymbol{\nabla}[X_k] - \frac{[X_k]}{D^\mathrm{e}_{k,\mathrm{Kn}}}\frac{B_\mathrm{g}}{\mu}\boldsymbol{\nabla} p. \tag{4.4}$$

Here, $[X_T] = \frac{p}{RT}$ is the total molar concentration, B_g is the permeability, and μ is the mixture viscosity. The DGM combines the effects of ordinary multicomponent diffusion (gas-gas collisions), Knudsen diffusion (gas-wall collisions), and pressure-driven Darcy flow. The ordinary diffusion coefficent $D^e_{k\ell}$ and the Knudsen diffusion coefficient $D^e_{k,\mathrm{Kn}}$ depend on the binary gas-to-gas diffusion coefficients (evaluated from kinetic theory) and the physical porous media properties. These properties include porosity ϕ, average pore radius r_p, tortuosity τ_g, and catalyst specific surface area A_s.

Heterogeneous chemistry is represented by a reaction mechanism describing CH_4-reforming on Ni-based catalysts. The mechanism used is taken from Hecht et al. [2] and contains 21 reversible elementary reactions (see Table 4.1) involving 6 gas-phase and 12 surface-adsorbed species. It has been validated experimentally for both steam and dry (CO_2) reforming for Ni-YSZ anodes at 800°C [46]. Because the mechanism is based on elementary reactions and describes all combinations of steam reforming, dry reforming, partial oxidation, and autothermal reforming, its applicability spans a far-broader range than the global reforming reactions often used in SOFC modeling.

Catalyst properties of porosity, tortuosity, specific catalyst surface area, pore size, particle size, and thickness are defined based on the RS-Type anode for incorporation into the catalytic reactor model. A tortuosity value of 3.1 and a specific catalyst surface area of 1080 cm^2/cm^3 was used. These values are based on previous studies of the RS-Type anode. Inlet conditions are described with a volumetric flow rate and fuel stream composition. A mixture of 50% CH_4/50% H_2O and 50% CH_4/50% CO_2 are used to represent the two reforming cases. Computations are performed for the same flow rates used in the SAE experiment; 75, 100, 150, and 200 sccm. Atmospheric pressure is assumed at the reactor outlet.

Table 4.1: Surface reaction mechanism for CH_4 on Ni [1].

	Reaction	A[a]	n	E[a]
1.	$H_2 + Ni(s) + Ni(s) \rightarrow H(s) + H(s)$	1.000E-02[b]	0.0	0.00
2.	$H(s) + H(s) \rightarrow Ni(s) + Ni(s) + H_2$	5.593E+19[b]	0.0	88.12
3.	$O_2 + Ni(s) + Ni(s) \rightarrow O(s) + O(s)$	1.000E-02[b]	0.0	0.00
4.	$O(s) + O(s) \rightarrow Ni(s) + Ni(s) + O_2$	2.508E+23[b]	0.0	470.39
5.	$CH_4 + Ni(s) \rightarrow CH_4(s)$	8.000E-03[b]	0.0	0.00
6.	$CH_4(s) \rightarrow Ni(s) + CH_4$	5.302E+15[b]	0.0	33.15
7.	$H_2O + Ni(s) \rightarrow H_2O(s)$	1.000E-01[b]	0.0	0.00
8.	$H_2O(s) \rightarrow Ni(s) + H_2O$	4.579E+12[b]	0.0	62.68
9.	$CO_2 + Ni(s) \rightarrow CO_2(s)$	1.000E-05[b]	0.0	0.00
10.	$CO_2(s) \rightarrow Ni(s) + CO_2$	9.334E+07[b]	0.0	28.80
11.	$CO + Ni(s) \rightarrow CO(s)$	5.000E-01[b]	0.0	0.00
12.	$CO(s) \rightarrow Ni(s) + CO$	4.041E+11[b]	0.0	112.85
		$\varepsilon_{CO(s)}$		-50.0[c]
13.	$O(s) + H(s) \rightarrow OH(s) + Ni(s)$	5.000E+22	0.0	97.90
14.	$OH(s) + Ni(s) \rightarrow O(s) + H(s)$	2.005E+21	0.0	37.19
15.	$OH(s) + H(s) \rightarrow H_2O(s) + Ni(s)$	3.000E+20	0.0	42.70
16.	$H_2O(s) + Ni(s) \rightarrow OH(s) + H(s)$	2.175E+21	0.0	91.36
17.	$OH(s) + OH(s) \rightarrow O(s) + H_2O(s)$	3.000E+21	0.0	100.00
18.	$O(s) + H_2O(s) \rightarrow OH(s) + OH(s)$	5.423E+23	0.0	209.37
19.	$O(s) + C(s) \rightarrow CO(s) + Ni(s)$	5.200E+23	0.0	148.10
20.	$CO(s) + Ni(s) \rightarrow O(s) + C(s)$	1.418E+22	0.0	115.97
		$\varepsilon_{CO(s)}$		-50.0[c]
21.	$O(s) + CO(s) \rightarrow CO_2(s) + Ni(s)$	2.000E+19	0.0	123.60
		$\varepsilon_{CO(s)}$		-50.0[c]
22.	$CO_2(s) + Ni(s) \rightarrow O(s) + CO(s)$	3.214E+23	-1.0	86.50
23.	$HCO(s) + Ni(s) \rightarrow CO(s) + H(s)$	3.700E+21	0.0	0.0
		$\varepsilon_{CO(s)}$		-50.0[c]
24.	$CO + H(s) \rightarrow HCO(s) + Ni(s)$	2.338E+20	-1.0	127.98
25.	$HCO(s) + Ni(s) \rightarrow O(s) + CH(s)$	3.700E+24	-3.0	95.80
26.	$O(s) + CH(s) \rightarrow HCO(s) + Ni(s)$	7.914E+20	-3.0	114.22
27.	$CH_4(s) + Ni(s) \rightarrow CH_3(s) + H(s)$	3.700E+21	0.0	57.70
28.	$CH_3(s) + H(s) \rightarrow CH_4(s) + Ni(s)$	4.438E+21	0.0	58.83
29.	$CH_3(s) + Ni(s) \rightarrow CH_2(s) + H(s)$	3.700E+24	0.0	100.00
30.	$CH_2(s) + H(s) \rightarrow CH_3(s) + Ni(s)$	9.513E+22	0.0	52.58
31.	$CH_2(s) + Ni(s) \rightarrow CH(s) + H(s)$	3.700E+24	0.0	97.10
32.	$CH(s) + H(s) \rightarrow CH_2(s) + Ni(s)$	3.008E+24	0.0	76.43
33.	$CH(s) + Ni(s) \rightarrow C(s) + H(s)$	3.700E+21	0.0	18.80
34.	$C(s) + H(s) \rightarrow CH(s) + Ni(s)$	4.400E+22	0.0	160.49
35.	$O(s) + CH_4(s) \rightarrow CH_3(s) + OH(s)$	1.700E+24	0.0	88.30
36.	$CH_3(s) + OH(s) \rightarrow O(s) + CH_4(s)$	8.178E+22	0.0	28.72
37.	$O(s) + CH_3(s) \rightarrow CH_2(s) + OH(s)$	3.700E+24	0.0	130.10
38.	$CH_2(s) + OH(s) \rightarrow O(s) + CH_3(s)$	3.815E+21	0.0	21.97
39.	$O(s) + CH_2(s) \rightarrow CH(s) + OH(s)$	3.700E+24	0.0	126.80
40.	$CH(s) + OH(s) \rightarrow O(s) + CH_2(s)$	1.206E+23	0.0	45.42
41.	$O(s) + CH(s) \rightarrow C(s) + OH(s)$	3.700E+21	0.0	48.10
42.	$C(s) + OH(s) \rightarrow O(s) + CH(s)$	1.764E+21	0.0	129.08

[a] Arrhenius parameters for the rate constants written in the form: $k = A\exp(-E/RT)$. The units of A are given in terms of moles, centimeters, and seconds. E is in kJ/mol.
[b] Sticking coefficient
[c] Coverage dependent activation energy. Detailed definition may be found in Hecht et al. [1]
Total available surface site density is $\Gamma = 2.60 \times 10^{-9}$ mol/cm^2.

CHAPTER 5

RESULTS AND ANALYSIS

5.1 CO_2 Reforming vs. H_2O Reforming

The catalytic reactor model is used to evaluate product differences between dry-reforming and steam-reforming. As shown in Table 5.1, significantly different reformate compositions are predicted for the two types of reforming. However, for all four flowrate conditions, CH_4 conversion is 2% higher for steam-reforming than for dry-reforming. CH_4 conversion is defined as

$$CH_4 \text{ Conversion} = \frac{X_{In} - X_{Out}}{X_{In}}. \tag{5.1}$$

Table 5.1: Catalyst reactor results: product mole fractions at 100 sccm total flow rate.

Reforming Type Reforming Type	H_2	H_2O	CO	CO_2	CH_4	CH_4 Conversion
Dry	2.1%	4.9%	10.9%	39%	15.8%	68.4%
Steam	14.2%	40.3%	1%	2.6%	15%	70%

Final product mole fractions, however, are quite different between the two types of reforming. For steam reforming, a much higher percentage of H_2 is predicted in the exhaust stream. For dry reforming, CO dominates the product composition. This result is expected as the H_2/CO ratio for steam reforming is three and the ratio for dry reforming is one. On the basis of CH_4 conversion, steam and dry reforming are within 2% of each other. Additionally, it has been noted by Rostrup-Nielsen and Hansen that the kinetics of steam reforming are similar to those of dry reforming [47]. Though other product species vary greatly, this model-based analysis shows that the two chemical processes are similar enough to validate use of dry-reforming in place of steam-reforming for a comparison of anode reforming capabilities.

5.2 Experimental Repeatability

Repeatability results are provided in Figure 5.1(a) - Figure 5.1(e). Standard deviation for the three measurements is provided above each set of data points.

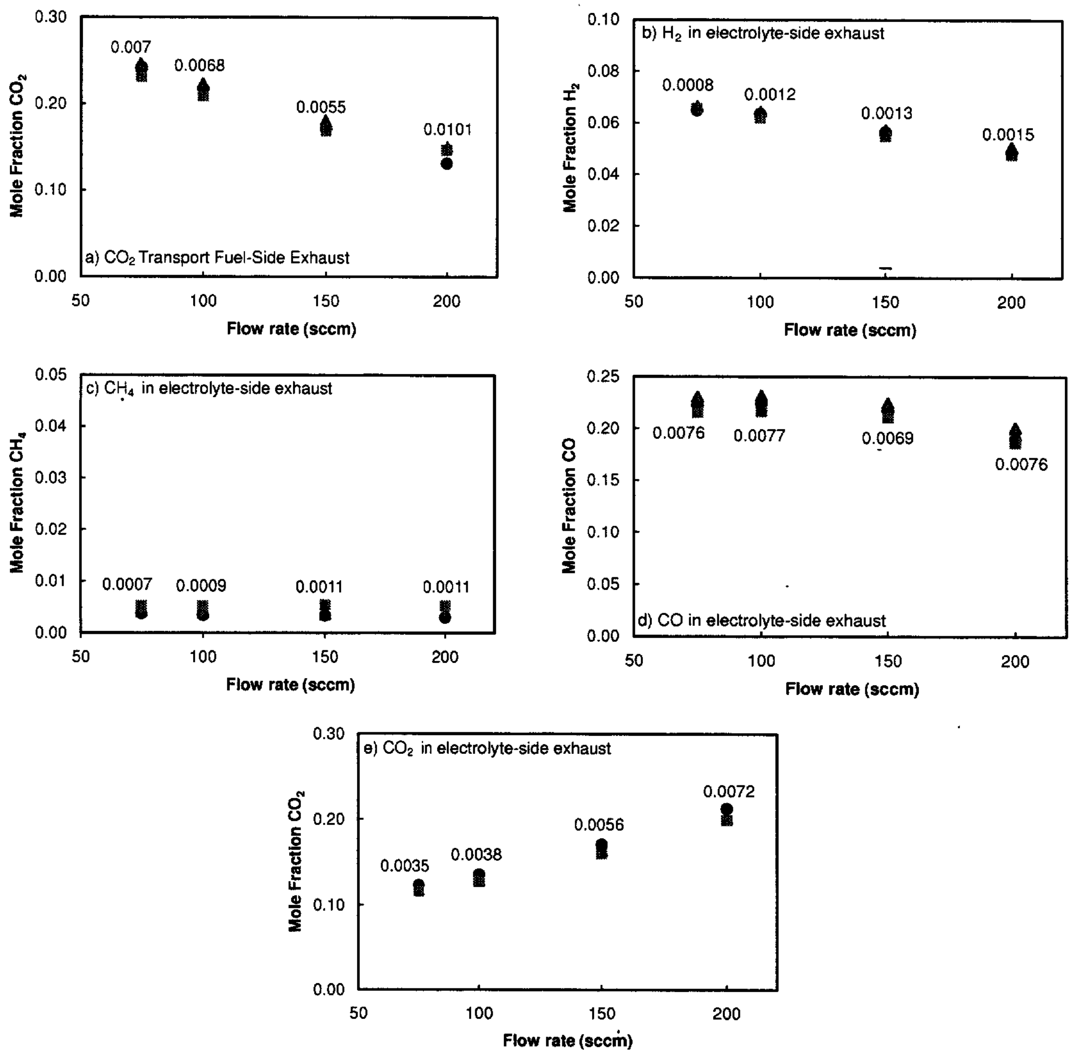

Figure 5.1: Mole fractions in exhaust streams for tests performed on three consecutive days on an RS-Type anode.

The repeatability tests show that the strongest matches are the H_2 (Figure 5.1(b))and

CH_4 (Figure 5.1(c)) measurements for the dry-reforming tests. The measurement with the worst repeatability is the 200 sccm condition for the CO_2 transport test (Figure 5.1(a)). Standard deviation of these measurements is 0.01 and is still acceptable. Repeatability appears to be better for the lowest flow rates and worsens with increasing flow rate. Overall, repeatability experiments demonstrate the reasonable precision of the measurement process in use.

5.3 Morphological and Material Characterization

The five anode materials and structures tested were characterized using a variety of tools as described in Section 3.3. SEM images are used to gain a general understanding of the material's pore structure and potential ability to transport gas through it. High-magnification SEM images are used to determine average particle size. Average pore size is determined using mercury porosimetry and porosity is determined via Archimedes' method. Thickness is another important parameter as it indicates the distance that a gas has to travel through the anode. These competing properties, while useful parameters in determining anode performance, do not provide a clear answer as to which material or structure will perform best.

5.3.1 SEM

SEM images taken of the cross-sections of the four materials studied are shown in Figure 5.2. Significant differences in the materials' microstructure is evident. Open porosity is a desirable trait for an anode material because it provides many pathways for gases to travel through. The RS-Type anode (a) has a more-open microstructure, with larger pores and particles than the other materials. Barrier layer (b) pores appear very fine and result in a more-closed microstructure. Color variations in the C-Type anode (c) highlight the differences in Ni and YSZ particles in the cermet anode. Large, dark, nickel particles are visible, as are smaller dark nickel particles.

YSZ particles appear as the lighter, small particles. While LSCM (d) contains many finer pores, the sizes of the pores and particles are smaller than those of the RS-Type anode.

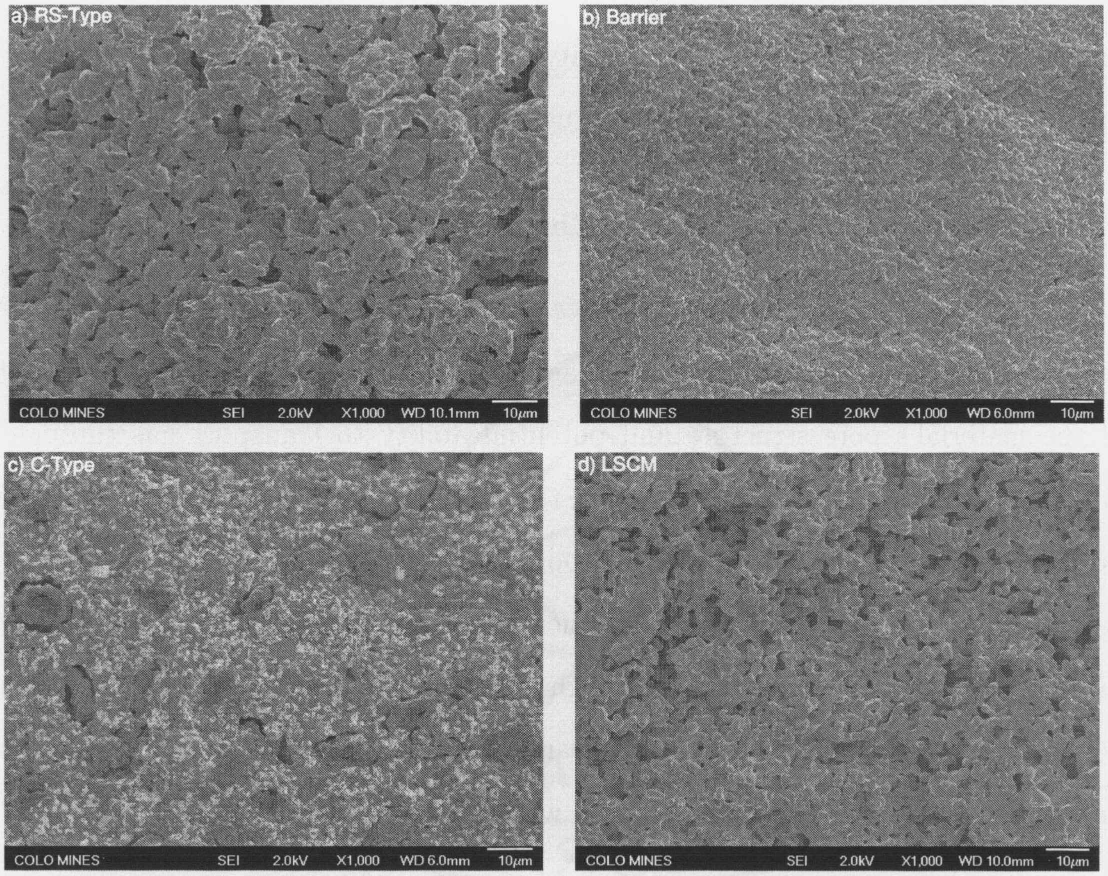

Figure 5.2: SEM images of cross-sectioned anodes.

5.3.2 Morphological Properties

A summary of anode morphological properties is provided in Table 5.2. From these properties, one might expect that the RS-Type anode will have the highest gas transport, followed by LSCM, C-Type, and then the barrier layer. Anode thickness, however, also plays a role in how much gas will diffuse through the anode. Gas transport is dependent upon all of these properties, thus it is difficult to tell which anodes will perform best. Though the RS-Type anode has the highest bulk porosity

Table 5.2: Anode morphological properties.

Anode	Porosity	Mean Pore Radius (μm)	Mean Particle Diameter (μm)	Thickness (mm)
RS-Type	43%	0.9	3	1448
C-Type	34.8%	0.1323	1.5	886.5
Barrier Layer	27%	0.1713	1.1	950
LSCM	36.8%	0.6763	2	1107

and largest mean pore diameter, its overall thickness is much higher than that of the other structures. These competing properties make it unclear as to which material will provide the most-facile gas transport.

5.4 Separated Anode Experiment Results

The Separated Anode Experiment is used to evaluate the gas transport and internal-reforming behaviors of the five anode materials and structures studied in this work. Results are divided into three groups: (1) a comparison of the nickel-based RS-Type and C-Type anodes; (2) a comparison of the behavior of the inert barrier layer and the barrier/RS-Type bi-layer; and (3) results for the nickel-free LSCM perovskite anode. Results from the RS-Type anode are included in all three sets of data for comparison.

5.4.1 Comparison of Nickel Anodes

CO_2 Transport

CO_2 mole fractions measured in the fuel-side exhaust stream (see Figure 5.3) provide a comparative measure on gas transport across the RS-Type and C-Type anodes. The amount of CO_2 in the fuel-side exhaust stream is much higher for the RS-Type anode than for the C-Type anode. These results indicate that the RS-Type anode is better able to promote gas transport despite being significantly thicker. These measurements are in agreement with the SEM images and liquid picnometry measurements shown in Figure 5.2 and Table 5.2, respectively. The pore radius of the RS-Type anode is almost seven times larger than that of the C-Type anode and is another contributor to higher transport.

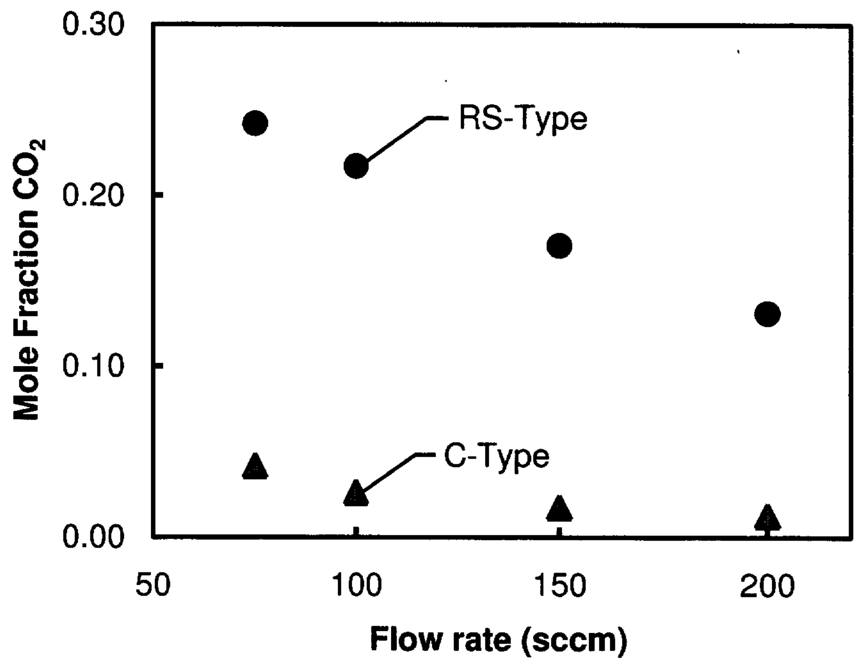

Figure 5.3: CO_2 mole fraction in fuel-side exhaust stream for RS-Type and C-Type anodes.

CH_4 Dry Reforming

The electrolyte-side exhaust streams for methane dry reforming over the RS-Type and C-Type anodes are shown in Figure 5.4. Reactant species are in Figure 5.4(a) and Figure 5.4(b); product species are in Figure 5.4(c) and Figure 5.4(d). The results shown in Figure 5.4(a) indicate that trace amounts of CH_4 remain in the exhaust stream for both anodes. The CH_4 is being consumed by catalytic reforming reactions within the nickel structures. More CO_2 is detected in the electrolyte exhaust stream for the C-Type anode than the RS-Type anode, in keeping with the gas-transport results, as the C-Type anode has a tighter microstructure reducing CO_2 diffusion into the anode structure. As for the reactants, significant differences exist between the H_2 and CO mole fractions for the anodes. A much-higher mole fraction of hydrogen is observed for the CoorsTek anode than for FCT's anode, but the CO mole fractions are much closer together. This may be due to the reverse water-gas shift reaction:

$$CO_2 + H_2 \rightarrow CO + H_2O.$$

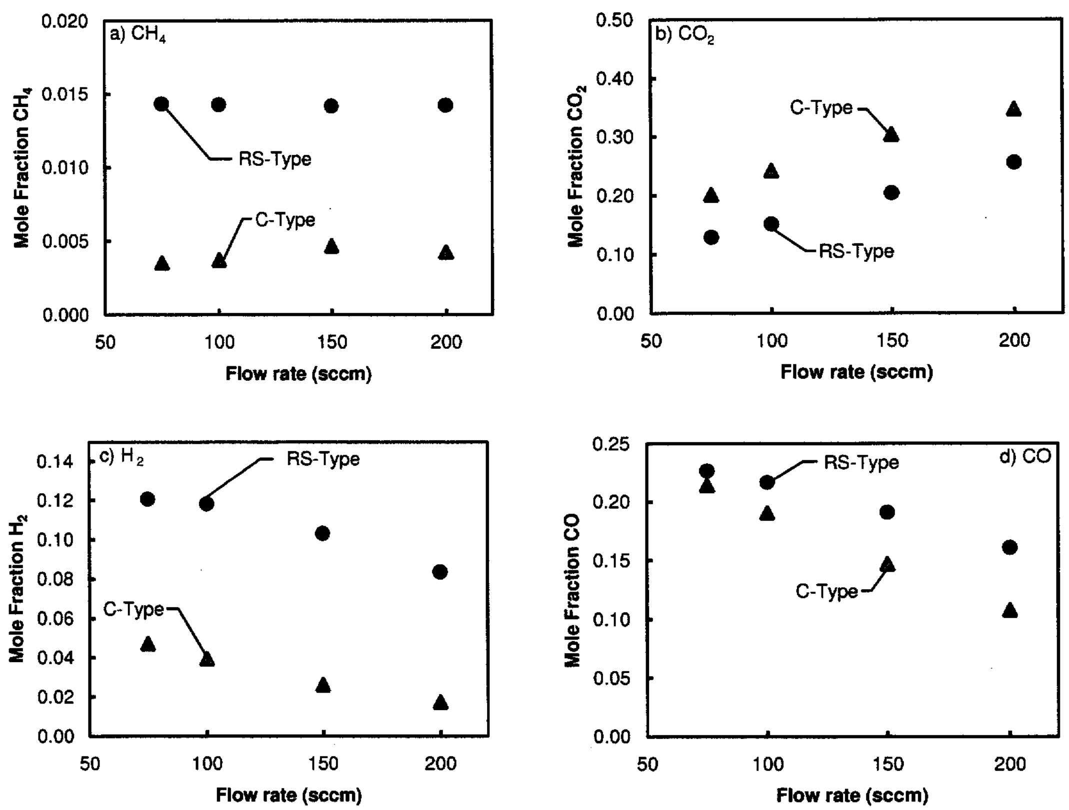

Figure 5.4: Electrolyte-exhaust mole fractions during dry-reforming of CH_4 within RS-Type and C-Type anodes.

As more CO_2 is present in the C-Type anode electrolyte stream, higher conversion of H_2 to H_2O may be occuring in this anode. Since the water content of the exhaust stream is not measured, it cannot be determined if the exhaust stream of the C-Type anode carries a higher steam content. All other indicators, however, demonstrate that a reverse water-gas shift has occurred.

A comparison of the RS-Type anode and the more conventional C-Type anode reveals that the more-open microstructure of the RS-Type anode results in higher syngas concentrations in the electrolyte exhaust streams, translating to higher syngas amounts at the triple-phase boundaries in an operating SOFC. Because the reactants are able to diffuse more freely through the RS-Type anode structure, more CH_4 can be reformed to H_2 and CO than for the C-Type structure.

5.4.2 Comparison of Barrier Layer and RS-Type Anodes

CO_2 Transport

The results of the gas transport tests for a barrier layer and a barrier layer combined with an RS-Type anode (bi-layer) are shown in Figure 5.5.

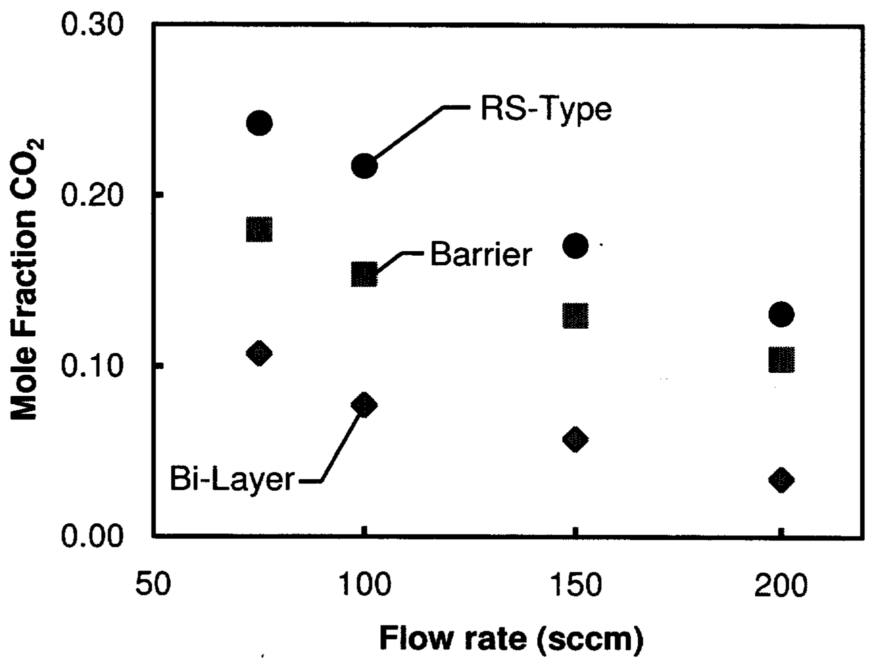

Figure 5.5: CO_2 mole fraction in fuel-side exhaust stream for RS-Type anode, YSZ barrier layer, and CoorsTek/barrier bi-layer.

RS-Type anode results are also shown for comparison. As expected from the porosity data, the RS-Type anode has the highest gas transport, followed by the the barrier layer, and then the combination of the two. An increased total cross-sectional thickness of the barrier layer and RS-Type anode result in lower gas transport. In addition to having a lower porosity than the RS-Type anode, the barrier layer also has smaller pores and particles. However, lower gas transport within a barrier layer is desirable for slowing the flux of hydrocarbon fuel onto a catalytic surface.

CH_4 Dry Reforming

Electrolyte-side exhaust mole fractions for dry reforming tests on the barrier layer anodes are provided in Figure 5.6.

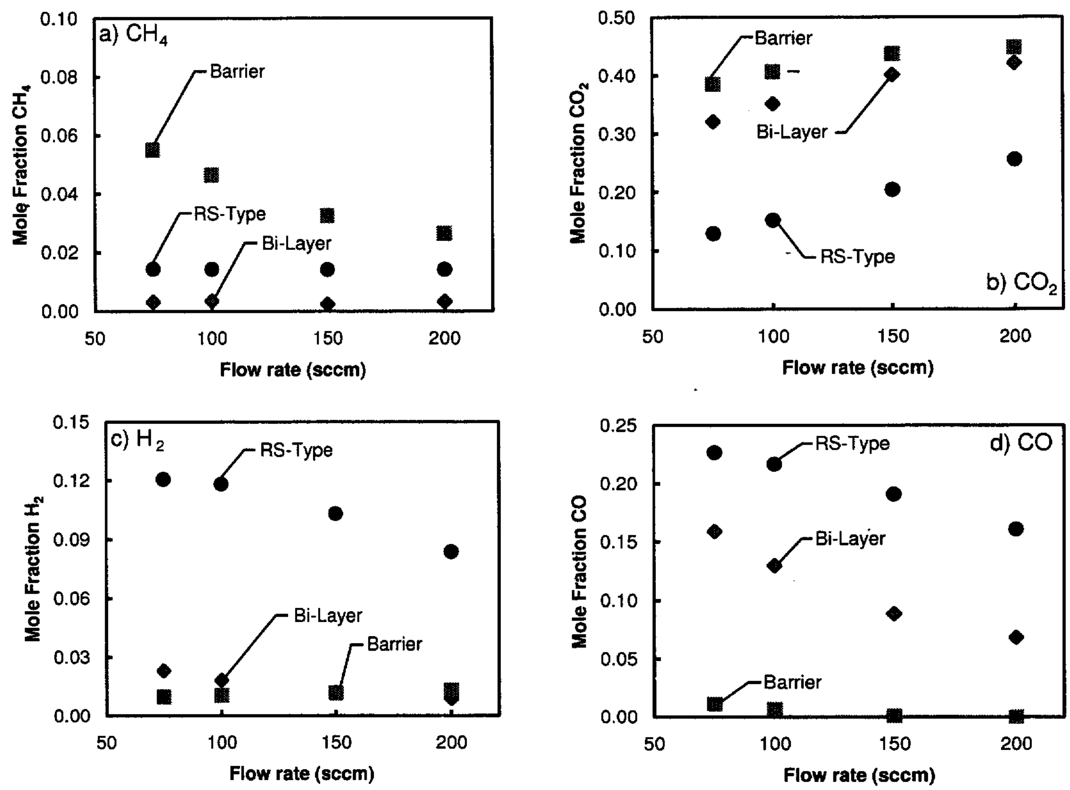

Figure 5.6: Electrolyte-exhaust mole fractions during dry reforming of CH_4 within RS-Type anode, YSZ barrier layer, and RS-Type/barrier bi-layer structures.

Again, reforming reactants are in Figure 5.6(a) and Figure 5.6(b), while products are in Figure 5.6(c) and Figure 5.6(d). The inert barrier layer performs as expected. While some CH_4 and CO_2 are transported through the barrier layer, very little methane reforming occurs, as the YSZ material is not an active catalyst for dry-reforming of CH_4. Virtually no H_2 or CO is present in the exhaust stream as shown in Figure 5.6(c) and Figure 5.6(d).

For the anode/barrier bi-layer, a small amount of CH_4 is present in the electrolyte exhaust. While this and a low H_2 concentration imply low gas transport from the fuel side to the electrolyte side, the high CO content in the electrolyte exhausts indicates that significant fuel conversion is occurring (Figure 5.6(d)). As CO_2 is present in the bi-layer electrolyte exhaust stream, the reverse water-gas shift may also be occurring here.

5.4.3 Comparison of LSCM and RS-Type Anodes

CO_2 Transport

Gas transport experiment results for the perovskite anode are shown in Figure 5.7. The RS-Type anode results are provided for comparison.

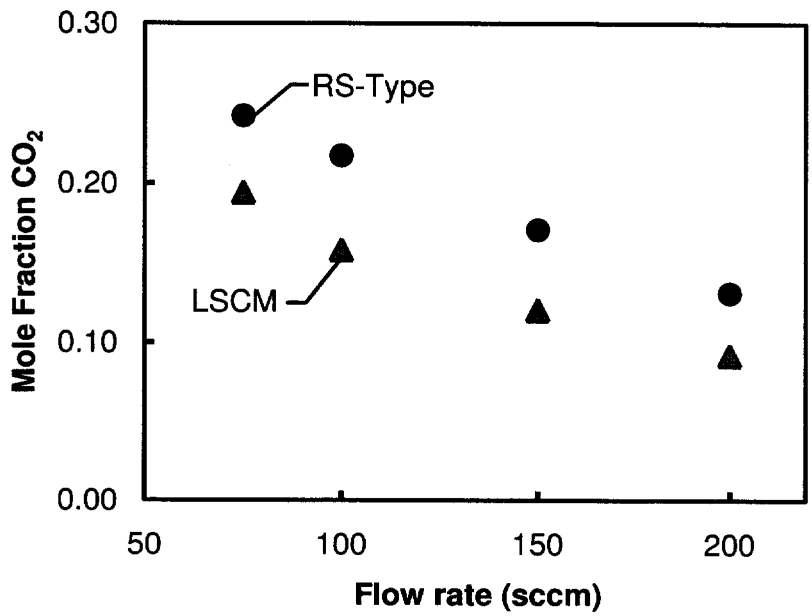

Figure 5.7: CO_2 mole fraction in fuel-side exhaust stream for RS-Type and LSCM anodes.

Again, gas transport through the LSCM anode is lower than the RS-Type anode. Material properties such as porosity, pore size, and particle size indicate that this is the expected result. While gas transport is lower for LSCM than for the RS-Type anode, LSCM gas transport is reasonable, implying that the LSCM microstructure is adequate from the perspective of gas transport.

CH_4 Dry Reforming

CH_4 dry reforming experiment results for the LSCM and RS-Type anodes are shown in Figure 5.8.

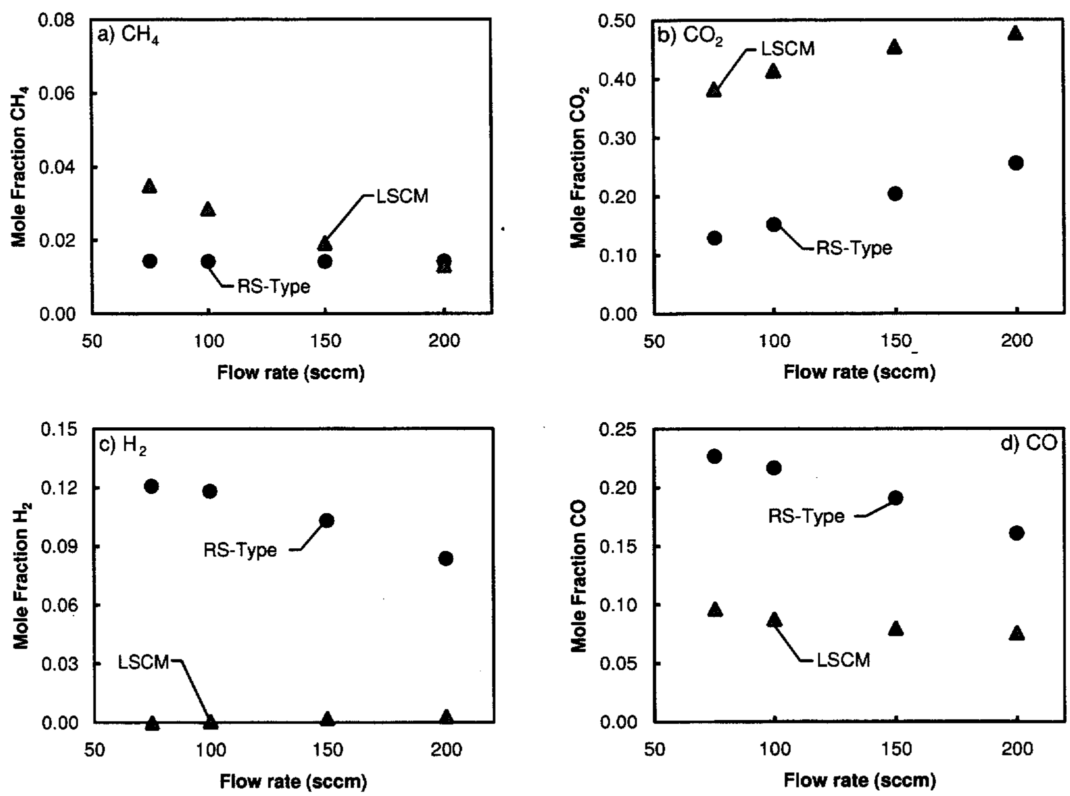

Figure 5.8: Electrolyte-exhaust mole fractions during dry reforming of CH_4 within LSCM and RS-Type structures.

Figure 5.8(a) shows that some CH_4 has diffused through the LSCM anode to the electrolyte-side, and Figure 5.8(b) shows that most of the CO_2 remains on the electrolyte-side. No H_2 is measured in the exhaust stream (Figure 5.8(c)), despite the fact that the inlet stream contained 3.5% H_2. Figure 5.8(d) reveals that significant CO is produced during the experiment.

Though LSCM does not show significant catalytic activity for CH_4 reforming, it does show activity for the reverse water-gas shift reaction since CO is generated and H_2 is consumed. The catalytic activity of LSCM for the reverse water-gas shift has been reported on by Tao et al. [48]. It was reported that the general reaction was

$$CH_4 + 3CO_2 \rightarrow 2H_2O + 4CO,$$

and the end products were steam and CO rather than H_2 and CO. These results, combined with the previous work of Tao, indicate that, in order for LSCM to be a viable anode for operation on hydrocarbon fuels, the catalytic activity for breaking C-H bonds must be increased.

CHAPTER 6

CONCLUSIONS

The Separated Anode Experiment has been developed to provide a basis for comparing the gas-transport and fuel-reforming attributes of different SOFC anodes and structures. These processes are tightly coupled and difficult to understand with traditional electrochemical testing procedures. Though previous studies have been performed using this experiment, it has been further improved upon and developed in this work. In this study, five different anodes were evaluated and compared: a reaction-sintered Ni-YSZ anode, a conventional Ni-YSZ anode with AFL, an inert barrier layer, an RS-Type/barrier bi-layer, and a nickel-free perovskite anode.

The RS-Type anode shows the highest gas transport and internal reforming capabilities due to its more-open pore structure. The C-Type anode, while demonstrating an ability for methane reforming, shows very low gas transport as a result of its finer, more-closed microstructure. The inert barrier layer has lower gas transport than the RS-type anode and negligible reforming capabilities, both of which are expected results. As a result of the increased thickness, the RS-Type/barrier bi-layer demonstrates lower gas transport than both of its original components, but has higher internal reforming capabilities than the barrier layer alone. Reforming capabilities could be increased by improving the microstructure of the barrier layer. The LSCM perovskite anode, while demonstrating catalytic activity for the reverse water-gas shift, has very little methane-reforming catalytic activity. Its ability to transport gas, however, is sufficient.

Although steam is an important product of electrochemistry, dry reforming has been used in this study in place of steam reforming due to experimental constraints. A comparison of the two types of reforming has been performed using a plug-flow reactor model. Model results show that, while H_2 and CO product mole fractions vary, total CH_4 conversion is approximately equal.

6.1 Experimental Improvements

Some weaknesses exist in this experimental setup and have been identified as areas for improvement. Mass spectrometry is currently used for quantification of exhaust species. Though the repeatability of this technique has been verified in this study, it is not as accurate as other measurement methods for quantification. Gas chromatography would be a better measurement technique to use for this application. An Agilent MicroGC has been purchased for this task and will be put into use in future experiments. By utilizing a GC, the overlap of CO and N_2 signals will no longer be a problem. Additionally, a shorter distance between the experiment and measurement device will likely minimize the opportunities for leaks to appear.

Additionally, since steam is a major product of electrochemistry, its addition to the inlet stream must be made accurate and incorporated into the experiments. The previous method of steam addition was through the use of a bubbler heated to a temperature corresponding to a desired mole fraction of steam. Through extensive testing as part of this work, this method proved to be extremely unreliable. Incorporation of a vaporizer into the experimental setup is recommended. Development of a reliable vaporizer is currently being conducted at the Colorado Fuel Cell Center.

Measurement of steam mole fraction of the experimental exhaust is also recommended, especially for experiments involving steam reforming. It is an important product in reforming reactions and would also help determine whether the reverse water-gas shift reaction is occurring in certain situations. A dewpoint hygrometer such as the one produced by Rotronic would be useful.

6.2 Future Work

Future work for the SAE involves expanding gas-transport and CH_4 steam-reforming tests to different anode materials. These materials will include a catalyst-coated barrier layer and new perovskite anodes. The current barrier layer will be improved to obtain higher porosity and will then be coated with Rh particles. A multi-phase perovskite anode currently under development at the CFCC will also be investigated with the SAE. This anode contains LSCM, SLT, and YSZ. It is designed to have higher catalytic activity for hydrocarbon reforming.

Future work will also include the development of a computational model. Efforts will be made to match the computational model predictions with experimental results. Carbon and hydrogen element balances will be performed on experimental data. Sensitivity to properties such as tortuosity, pore size, particle size, and catalyst surface area will be analyzed. Improvements to the computational model may include alterations to the heterogeneous kinetic mechanism being used for chemistry. This mechanism, however, will only be applicable for anodes containing nickel.

With experimental improvements and model development, a final goal for the SAE is to utilize it for microstructure optimization of anodes. An optimal SOFC anode must possess a balance between gas transport and reforming capabilities with a minimization of carbon deposition. A finely-tuned model can aid in determining the best balance.

REFERENCES CITED

[1] R. O'Hayre, S.-W. Cha, W. Colella, and F.B. Prinz. *Fuel Cell Fundamentals.* John Wiley & Sons, Inc., Hoboken, NJ, 2006.

[2] E.S. Hecht, G.K. Gupta, H. Zhu, A.M. Dean, R.J. Kee, L. Maier, and O. Deutschmann. Methane reforming kinetics within a Ni-YSZ SOFC anode support. *Applied Catalysis A*, 295:40–51, 2005.

[3] J.M. Daggett. Ethanol transport and chemistry in Ni/YSZ anodes for solid oxide fuel cell applications. Master's thesis, Colorado School of Mines, 2008.

[4] Y. Lin, Z. Zhan, and S.A. Barnett. Improving the stability of direct-methane solid oxide fuel cells using anode barrier layers. *Journal of Power Sources*, 158:1313 – 1316, 2006.

[5] M. Pillai, Y. Lin, H. Zhu, R.J. Kee, and S.A. Barnett. Stability and coking of direct-methane solid oxide fuel cells: Effect of CO_2 and air additions. *Journal of Power Sources*, 195:271–279, 2010.

[6] H. Zhu, A.M. Colclasure, R.J. Kee, Y. Lin, and S.A. Barnett. Anode barrier layers for tubular solid-oxide fuel cells with methane fuel streams. *Journal of Power Sources*, 161:413–419, 2006.

[7] Zhongliang Zhan and Scott A. Barnett. An octane-fueled solid oxide fuel cell. *Science*, 308:844–847, 2005.

[8] P.K. Cheekatamarla, Caine M. Finnerty, and Jun Cai. Internal reforming of hydrocarbon fuels in tubular solid oxide fuel cells. *International Journal of Hydrogen Energy*, 33:1853–1858, 2008.

[9] J. Sfeir, P.A. Buffat, P. Mockli, N. Xanthopoulos, R. Vasquez, J.J. Mathieu, J. Van herle, and K.R. Thampi. Lanthanum chromite based catalysts for oxidation of methane directly on SOFC anodes. *Journal of Catalysis*, 202:229–244, 2001.

[10] B.A. Boukamp. The amazing perovskite anode. *Nature Materials*, 2:294–296, 2003.

[11] S. Tao and J.T.S. Irvine. A redox-stable efficient anode for solid-oxide fuel cells. *Nature Materials*, 2:320–323, 2003.

[12] D.M. Bastidas, S. Tao, and J.T.S. Irvine. A symmetrical solid oxide fuel cell demonstrating redox stable perovskite electrodes. *Journal of Materials Chemistry*, 16:1603–1605, 2006.

[13] G. Corre, G. Kim, M. Cassidy, R.J. Gorte, J.M. Vohs, and J.T.S. Irvine. Microstructural studies and performance of impregnated manganese containing perovskite solid oxide fuel cell anodes. *ECS Transactions*, 25:2201–2211, 2009.

[14] M.K. Bruce, M. van den Bossche, and S. McIntosh. The influence of current density on the electrocatalytic activity of oxide-based direct hydrocarbon SOFC anodes. *Journal of The Electrochemical Society*, 155:B1202–B1209, 2008.

[15] S.W. Tao and J.T.S. Irvine. Catalytic properties of the perovskite oxide $La_{0.75}Sr_{0.25}Cr_{0.5}Fe_{0.5}O_{3-\delta}$ in relation to its potential as a solid oxide fuel cell anode material. *Chemistry of Materials*, 16:4116–4121, 2004.

[16] Q. X. Fu, F. Tietz, and D. Stöver. $La_{0.4}Sr_{0.6}Ti_{1-x}Mn_xO_{3-\delta}$ perovskites as anode materials for solid oxide fuel cells. *Journal of The Electrochemical Society*, 153:D74–D83, 2006.

[17] A. Ovalle, J.C. Ruiz-Morales, J. Canales-Vazquez, D. Marrero-Lopez, and J.T.S. Irvine. Mn-substituted titanates as efficient anodes for direct methane SOFCs. *Solid State Ionics*, 177:1997–2003, 2006.

[18] M. Pillai, I. Kim, D. Bierschenk, and S.A. Barnett. Fuel-flexible operation of a solid oxide fuel cell with $Sr_{0.8}La_{0.2}TiO_3$ support. *Journal of Power Sources*, 185:1086–1093, 2008.

[19] Chao Su, Yuzhou Wu, Wei Wang, Yao Zheng, Ran Ran, and Zongping Shao. Assessment of nickel cermets and $La_{0.8}Sr_{0.2}Sc_{0.2}Mn_{0.8}O_3$. *Journal of Power Sources*, 195:1333–1343, 2010.

[20] P. Blennow, K.K. Hansen, L.R. Wallenberg, and M. Mogensen. Electrochemical characterization and redox behavior of Nb-doped $SrTiO_3$. *Solid State Ionics*, 180:63–70, 2009.

[21] M.J. Escudero, J.T.S. Irvine, and L. Daza. Development of anode material based on La-substituted $SrTiO_3$ perovskites doped with manganese and/or gallium for SOFC. *Journal of Power Sources*, 192:43–50, 2009.

[22] Y.-H. Huang, R.I. Dass, J.C. Denyszyn, and J.B. Goodenough. Synthesis and Characterization of $Sr_2MgMoO_{6-\delta}$. *Journal of The Electrochemical Society*, 153:A1266–A1272, 2006.

[23] S. Park, J.M. Vohs, and R.J. Gorte. Direct oxidation of hydrocarbons in a solid-oxide fuel cell. *Nature (London)*, 404:265–266, 2000.

[24] H. He, J.M. Vohs, and R.J. Gorte. Effect of synthesis conditions on the performance of Cu-CeO_2-YSZ anodes in SOFCs. *Journal of The Electrochemical Society*, 150:A1470–A1475, 2003.

[25] T. Kim, G. Liu, M. Boaro, S.-I. Lee, J.M. Vohs, R.J. Gorte, O.H. Al-Madhi, and B.O. Dabbousi. A study of carbon formation and prevention in hydrocarbon-fueled SOFC. *Journal of Power Sources*, 155:231–238, 2006.

[26] N.M. Galea, D. Knapp, and T. Ziegler. Density functional theory studies of methane dissociation on anode catalysts in solid-oxide fuel cells: Suggestions for coke reduction. *Journal of Catalysis*, 247:20–33, 2007.

[27] A. Hornés, D. Gamarra, G. Munuera, J.C. Conesa, and A. Martínez-Arias. Catalytic properties of monometallic copper and bimetallic copper-nickel systems combined with ceria and Ce-X (X = Gd, Tb) mixed oxides applicable as SOFC anodes for direct oxidation of methane. *Journal of Power Sources*, 169:9–16, 2007.

[28] S.-I. Lee, J.M. Vohs, and R.J. Gorte. A Study of SOFC Anodes Based on Cu-Ni and Cu-Co Bimetallics in CeO_2-YSZ. *Journal of The Electrochemical Society*, 151:A1319–A1323, 2004.

[29] S.-I. Lee, K. Ahn, J.M. Vohs, and R.J. Gorte. Cu-Co Bimetallic Anodes for Direct Utilization of Methane in SOFCs. *Electrochemical and Solid-State Letters*, 8:A48–A51, 2005.

[30] A. Ringuedé, D.P. Fagg, and J.R. Frade. Electrochemical behaviour and degradation of (Ni,M)/YSZ cermet electrodes (M=Co,Cu,Fe) for high temperature applications of solid electrolytes. *Journal of the European Ceramic Society*, 24:1355–1358, 2004.

[31] C.M. Grgicak, M.M. Pakulska, J.S. O'Brien, and J.B. Giorgi. Synergistic effects of $Ni_{1-x}Co_x$-YSZ and $Ni_{1-x}Cu_x$-YSZ alloyed cermet SOFC anodes for oxidation of hydrogen and methane fuels containing H_2S. *Journal of Power Sources*, 183:26–33, 2008.

[32] A.J. Bard and L.R. Faulkner. *Electrochemical Methods: Fundamentals and Applications.* John Wiley & Sons, Inc., Hoboken, NJ, 2 edition, 2001.

[33] A.M. Sukeshini, B. Habibzadeh, B.P. Becker, C.A. Stoltz, B.W. Eichhorn, and G.S. Jackson. Electrochemical oxidation of H_2, CO, and CO / H_2 mixtures on patterned Ni anodes on YSZ electrolytes. *Journal of the Electrochemical Society*, 153:A705–A717, 2006.

[34] M. Liu, X. Lu, and P. Faguy. *In-situ* characterization of electrode reactions in solid oxide fuel cells. *Electrochemical Society Proceedings*, 2003-07:1132–1146, 2003.

[35] M.B. Pomfret, D.A. Steinhurst, D.A. Kidwell, and J.C. Owrutsky. Thermal imaging of solid oxide fuel cell anode processes. *Journal of Power Sources*, 195:257–262, 2010.

[36] K. Yashiro, K. Takeda, T. Taura, T. Otake, A. Kaimai, Y. Nigara, T. Kawada, and J. Mizusaki. *In-situ* observation of deposited carbon on anode for solid oxide fuel cells. *Electrochemical Society Proceedings*, 2003-07:714–719, 2003.

[37] R. Swartzlander and W.G. Coors. Preparation of yttria-stabilized zirconia reaction sintered products. United States Patent 20070176332, 2007.

[38] D. Storjohann, J. Daggett, N.P. Sullivan, H. Zhu, R.J. Kee, S. Menzer, and D. Beeaff. Fabrication and evaluation of solid-oxide fuel cell anodes employing reaction-sintered yttria-stabilized zirconia. *Journal of Power Sources*, 193:706–712, 2009.

[39] E. Hecht. Internal reforming of methane in a nickel-yttria stabilized zirconia solid oxide fuel cell anode. Master's thesis, Colorado School of Mines, 2005.

[40] G.K. Gupta. *Analysis of gas-phase and catalytic kinetics in solid oxide fuel cells.* PhD thesis, Colorado School of Mines, 2007.

[41] National Institute of Standards and Technology. NIST Chemistry WebBook. `http://webbook.nist.gov/chemistry`, February 2010.

[42] Ronald E. Loehman. *Characterization of Ceramics.* Butterworth-Heinemann, Stoneham, MA, 1993.

[43] D.G. Goodwin. Chemical Vapor Deposition XVI and EUROCVD 14. In M. Allendorf, F. Maury, and F. Teyssandier, editors, *The Electrochemical Society, Proceedings Series*, volume 2003-08, page 155, 2003.

[44] R.J. Kee, M.E. Coltrin, and P. Glarborg. *Chemically Reacting Flow: Theory and Practice.* John Wiley, Hoboken, NJ, 2003.

[45] E. Mason and A. Malinauskas. *Gas Transport in Porous Media: The Dusty-Gas Model.* American Elsevier, New York, 1983.

[46] H. Zhu, R.J. Kee, V.M. Janardhanan, O. Deutschmann, and D.G. Goodwin. Modeling elementary heterogeneous chemistry and electrochemistry in solid-oxide fuel cells. *Journal of The Electrochemical Society*, 152:A2427–A2440, 2005.

[47] J.R. Rostrup-Nielsen and J-H. Bak Hansen. CO_2-Reforming of methane over transition metals. *Journal of Catalysis*, 144:38–49, 1993.

[48] S. Tao, J.T.S. Irvine, and S.M. Plant. Methane oxidation at redox stable fuel cell electrode $La_{0.75}Sr_{0.25}Cr_{0.5}Mn_{0.5}O_{3-\delta}$. *Journal of Physical Chemistry B*, 110:21771–21776, 2006.

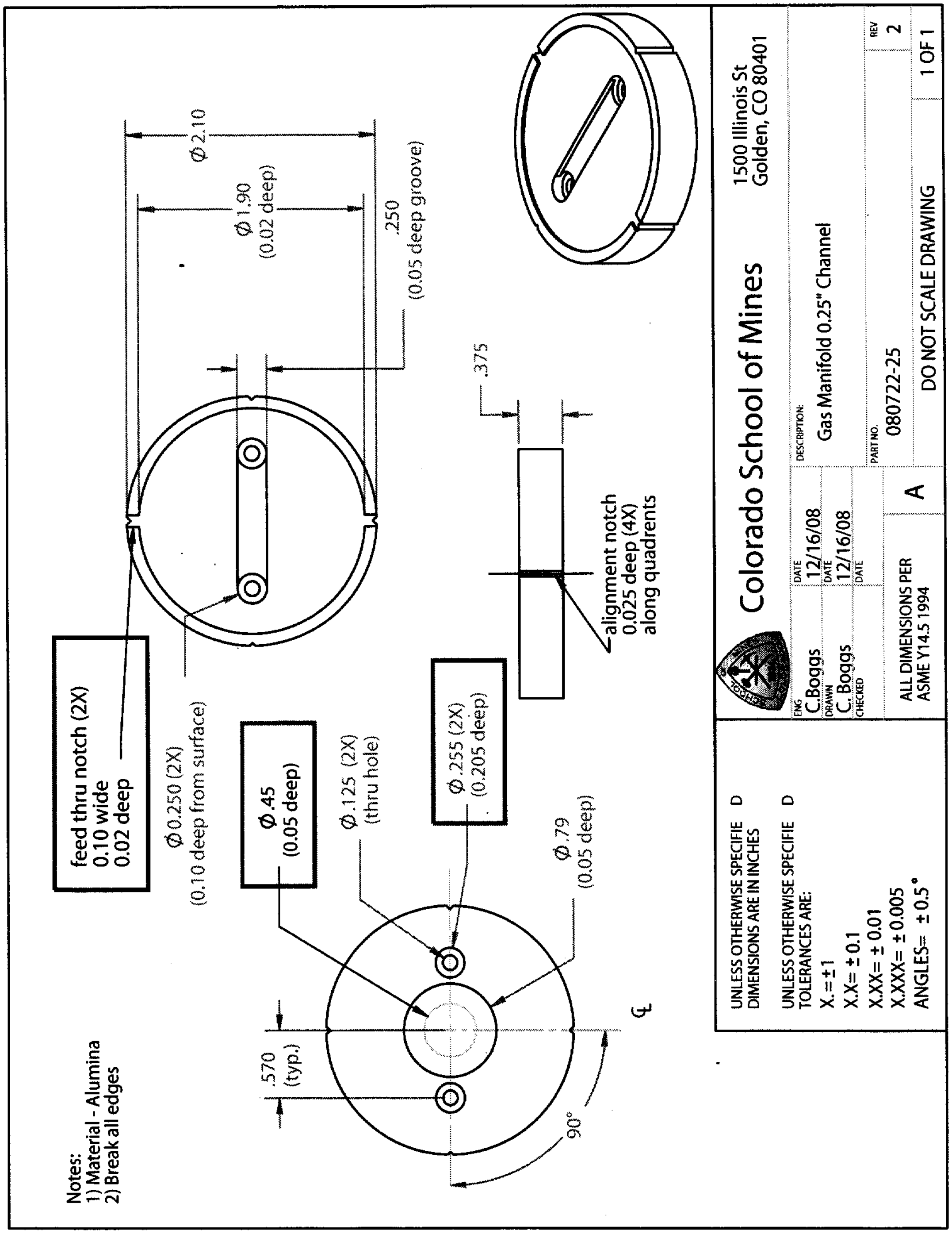

Figure A.1: This drawing not to scale .

APPENDIX B - FUEL UTILIZATION CALCULATIONS

Fuel utilization calculations are performed to understand the implications of the gas mixtures used in dry-reforming experiments. The percentage of the fuel supplied which would be used to sustain a typical SOFC current density is calculated using the following equations.

Assuming current density, i, of 0.45 $\mathrm{A/cm^2}$.

$$\dot{n}_{H_2,\text{req'd}} = \frac{i}{nF}, \tag{2.1}$$

where n is the number of moles of electrons per mole of H_2 (2) and F is Faraday's constant (96,400 Coulombs per mole). This means that 2e-6 moles of H_2 per second are needed to sustain a current density of 0.45 $\mathrm{A/cm^2}$. Since the dry reforming reaction of CH_4 is

$$\mathrm{CH_4 + CO_2 \rightarrow 2H_2 + 2CO},$$

a maximum number of two moles of hydrogen are available for every one mole of methane. Therefore,

$$\dot{n}_{H_2,\text{supplied}} = 2\dot{n}_{CH_4}. \tag{2.2}$$

The molar flow rate of CH_4 is calculated from experimental inlet conditions. For the case of 100 sccm with 20 mole % CH_4, there is a volumetric flow rate of 20 sccm of CH_4. The molar flow rate is calculated with the Ideal Gas Law,

$$\dot{n} = \frac{P\dot{V}}{RT}, \tag{2.3}$$

where R is the gas constant (0.082 L·atm/mol·K), T is the temperature (298 K), and P is the pressure (1 atm). The calculated molar flow rate of hydrogen is therefore

Table B.1: Fuel Utilization Values.

Flow Rate (sccm)	Fuel Utilization (%)
75	10
100	7.4
150	4.9
200	3.6

2.7e-5 moles H_2/sec. Fuel utilization is calculated with the equation,

$$Utilization = \frac{\dot{n}_{H_2,\text{req'd}}}{\dot{n}_{H_2,\text{supplied}}}. \tag{2.4}$$

A table of the calculated utilization values for every flow rate is shown in Table B.1. The table indicates that much more CH_4 is being supplied to the cell than is theoretically needed to sustain a current density of 0.45 A/cm^2. This calculation, however, assumes that all of the CH_4 supplied is reformed to H_2 fuel. Actual fuel utilization values would be higher.